PREDICTABILITY AND FINITE-TIME INSTABILITY OF THE NORTHERN WINTER CIRCULATION

Franco Molteni and T.N.Palmer
ECMWF, Shinfield Park, Reading, UK

Abstract

The finite-time instability and associated predictability of atmospheric circulations are defined in terms of the largest singular values, and associated singular vectors, of the linear evolution operator determined from given equations of motion. These quantities are calculated in both a barotropic and a 3-level quasi-geostrophic model, using as basic states realistic large-scale northern wintertime flows representing the climatological state, regime composites, and specific realisations of these regimes. For time-invariant basic states, the singular vectors are compared with the corresponding normal mode solutions; it is shown that the perturbations defined (at the initial time) by the singular vectors have much larger growth rates than the normal modes, and possess a more localised spatial structure.

The regimes studied have opposite values of the Pacific/North American index, and growth rates for the barotropic basic states appear to confirm earlier studies that the barotropic instability of the negative PNA states may be larger than the corresponding positive PNA states. The evolution of the singular vector perturbations, with emphasis on the vertical structure, is compared for time-evolving and time-invariant baroclinic basic states; the effects of nonlinearity are also discussed. It is shown that, in the baroclinic model, interactions between synoptic-scale eddies in the time-evolving basic state and in the perturbation field are a fundamental process which may lead to substantial transitions in the large-scale circulation. Therefore, results obtained from linear calculations using very smooth basic states cannot properly account for the predictability of a given regime.

These results form the basis of a technique used to initialise ensembles of forecasts made with a primitive equation model, described in the companion paper (*Mureau et al.*, 1992).

1. INTRODUCTION

The predictability of a dynamical system is determined by the divergence of trajectory segments whose starting points are close. For chaotic systems, initially close trajectories diverge asymptotically at an exponential rate given by the positive Lyapunov exponents (e.g. *Parker and Chua*, 1989). These exponents characterise the dynamical system from a global (phase-space) point of view. However, as the analysis of the simplest chaotic models shows, the degree of divergence of finite segments of trajectory depends strongly on the position of the starting points in the attractor set. Moreover, finite-time divergence rates need not be exponential and can be much larger than those given by the Lyapunov exponents (e.g. *Mukougawa et al.*, 1991).

As first described in a meteorological context by *Lorenz* (1965), divergence-rate exponents for finite trajectory portions are given by the singular values of the resolvent, $\boldsymbol{A}$, of the linearised equations of the dynamical system integrated over the trajectory segment. The linear disturbances associated with these singular values are eigenfunctions of the product operator $\boldsymbol{A}^*\boldsymbol{A}$. In this paper we refer to these eigenvectors as singular vectors (hereafter SVs); we want to emphasise that, in general, they are not shape-preserving solutions of

the dynamical equations, even when linearised about a steady solution of the equations. In this sense they contrast with the eigenvectors of $\boldsymbol{A}$ which, for steady basic states, determine the familiar normal mode solutions. For non self adjoint $\boldsymbol{A}$ (always the case for realistic basic state flows) the largest singular value of $\boldsymbol{A}$ can be much larger than the largest eigenvalue.

SVs with the largest singular values can be described as optimal, in the sense that they maximise linear disturbance growth over a chosen integration period. Such optimal SVs have been calculated for a number of idealised basic states by *Farrell* (1988,1989) and in a barotropic model by *Lacarra and Talagrand* (1988), *Borges and Hartmann* (1991), *Yoden and Nomura* (1991). Unlike normal mode solutions, the SVs form a complete orthonormal basis set. Insofar as the optimal SVs describe an amplifying disturbance (eigenvalue of $\boldsymbol{A}^*\boldsymbol{A}>1$) which, over the optimisation time, can exceed normal-mode growth, we refer to growth associated with the optimal SV as finite-time instability.

In this paper, optimal SVs are calculated for composite circulation patterns representing northern winter climatology and some of the most important observed wintertime regimes. The SVs are calculated in both a barotropic model and a 3-level quasi-geostrophic (QG) model. In addition, SV calculations for flows which were chosen as particular realisations of such regimes are also studied.

A summary of relevant theory is given in section 2 and a brief description of the barotropic and QG models is given in section 3. In section 4 we discuss in some detail the normal mode and optimal SVs for the winter climatological flow, in both barotropic and baroclinic models. In section 5 we present a summary of similar calculations on basic states obtained from the cluster analysis of *Molteni et al.* (1990). The cluster centroids chosen for study here have opposite phases of the Pacifc/North American (PNA) index (*Wallace and Gutzler*, 1981). We compare results with estimates of the dependence of forecast skill on the sign of the PNA index (*Palmer*, 1988; *Molteni and Tibaldi*, 1990).

This paper is a companion to *Mureau et al.* (1992; hereafter MMP) on Monte Carlo forecasting with a primitive equation model. The techniques developed in this paper form the basis of a strategy to create an ensemble of initial states for a primitive equation forecast model. As such, finite-time instabilities from two of the periods used in MMP are studied in section 6 of this paper using the QG model. We compare the evolution of SVs on fixed and time-evolving basic states, and also compare the linear and nonlinear evolution of perturbation disturbances.

2. FINITE-TIME MEASURES OF INSTABILITY

Consider a real N-dimensional dynamical system with state-vector X, whose evolution equation is

$$\frac{dX}{dt} = F[X] \tag{1}$$

The evolution of a small perturbation δX is determined by the linearised counterpart of (1) which can be written as

$$\frac{d\delta X}{dt} = L\delta X \tag{2}$$

where L is the Jacobian of F evaluated at some time t. Integrating over some portion of trajectory for $t_0 \le t \le t_1$, we can write (2) in integral form

$$\delta X(t_1) = A(t_1,t_0)\ \delta X(t_0) \tag{3}$$

If the variations in the basic state between t_0 and t_1 are neglected, so that L is constant, one can write

$$A(t_1,t_0) = \exp\left(L(t_1-t_0)\right) \tag{4}$$

Given an inner product (...,..) , the adjoint A^* of A is defined by the relationship (valid for any vectors f, g):

$$(f, Ag) = (A^*f, g) \tag{5}$$

In all the calculations below, the state vector of our dynamical model can be written as a (2- or 3-dimensional) streamfunction field ψ. We have chosen a norm such that

$$E(t) = (\psi(t),\ \psi(t)) = \int_V \nabla\psi(t) \cdot \nabla\psi(t)\ dV \tag{6}$$

is (twice) the rotational kinetic energy of the flow integrated over the whole atmosphere. From (3),

$$E(t_1) = \left(A^*(t_1,t_0)\ A(t_1,t_0)\ \psi\ (t_0),\ \psi(t_0)\right) \tag{7}$$

Now whilst in general A is not symmetric (i.e. $A \neq A^*$), by construction the product operator A^*A is. Hence the eigenfunctions $\xi_i(t_0)$ of A^*A form a complete orthonormal basis Therefore, in order to find those (normalised) perturbations at t_0 that maximise rotational kinetic energy at t_1, $\psi(t_0)$ should be chosen proportional to the eigenvector of $A^*A(t_1,t_0)$ with largest eigenvalue. The associated eigenvalues are by definition equal to the squares of the singular values σ_i of A. Note that the time evolution $A(t_1,t_0)\xi_i(t_0)$ of

these eigenvectors are themselves eigenvectors of $\boldsymbol{A}(t_1,t_0)\boldsymbol{A}^*(t_1,t_0)$, and also form an orthonormal set. (For a general background to these results within a linear algebra context see e.g. *Noble and Daniel*, 1977.)

In conventional analysis of low-order systems, these singular values are evaluated in the limit $t_1-t_0\to\infty$, and their logarithms give the Lyapunov exponents of 1), which characterise many of the global properties of the associated attractor (see *Lorenz*, 1985). Positive Lyapunov exponents exist for low-dimensional models of large-scale atmospheric motion, indicating the existence of a strange attractor for atmospheric dynamics (e.g. *Legras and Ghil*, 1985; *Malguzzi et al.*, 1990). However, these exponents are of limited use for studies of the local predictability properties of the atmospheric attractor, i.e. of the dependence of perturbation growth on initial state. Moreover, any perturbation consistent with realistic uncertainties in the initial values of global atmospheric fields will become highly nonlinear before the limit $t_1-t_0\to\infty$ is reached.

With the analysis above, we can define an index of finite-time instability $I(t_1,t_0)$ as equal to the largest singular value of $\boldsymbol{A}$, so that

$$I(t_1,t_0) = \max_i(\sigma_i) = ||\boldsymbol{A}(t_1,t_0)|| \tag{8}$$

is the 2-norm of $\boldsymbol{A}$. The inverse of $I(t_1,t_0)$ can be taken as a measure of (linear) predictability. Because the eigenvectors of $\boldsymbol{A}$ do not form an orthogonal basis for the phase space of the linearised dynamics, error growth rates inferred from its singular values can be very much larger than those inferred from its eigenvalues (that is, by the growth rates of the normal modes ζ_i.) Consequently, predictability estimates made from the maximum normal mode growth rate can be erroneously optimistic.

In section 4 below, we present results from both the barotropic and QG models of the eigenvector sets $\xi(t_0)$, $\zeta(t_0)$, associated with the largest eigenvalues, and the time-evolution $\boldsymbol{A}(t,t_0)\xi(t_0)$, $\boldsymbol{A}(t,t_0)\zeta(t_0)$ for time-invariant basic states. By definition, the spatial structure of the evolution of the normal modes are given by the normal modes themselves. As far as the SVs are concerned, with constant basic states the fastest growing SV will tend to evolve into the fastest growing normal mode when the optimisation time tends to infinity. (In the following, a SV optimised for an n-day time interval, and evaluated at day m will be referred to as the n-day optimal SV at day m). Although in this paper we shall concentrate our attention on the fastest growing SV as an indicator of predictability on a hemispheric scale, a description of part of the spectrum of SVs for a 12-hour optimisation time is given in MMP, where the importance of higher-order eigenvectors for regional predictability will be discussed.

3. DESCRIPTION OF NUMERICAL MODELS

a) Formulation of the barotropic model

The barotropic model used in this study is a spectral model with global domain which integrates a prognostic equation for 300 hPa relative vorticity. The series of spherical harmonics used in the representation of horizontal fields has a triangular truncation at total wavenumber 21 (T21). The governing equation is

$$\frac{\partial \zeta}{\partial t} = -J(\psi, \zeta + f) - D_B(\zeta) \tag{9}$$

where ζ is relative vorticity, $f = 2\ \Omega \sin \phi$, ψ is streamfunction, J is the horizontal Jacobian and

$$D_B(\zeta) = \tau_B^{-1}\zeta + c_H \nabla^8 \zeta \tag{10}$$

The vorticity damping in Eq. 10 has a timescale τ_B of 10 days. The hyperdiffusion coefficient is given by

$$C_H = \tau_H^{-1}\, a^8\, (21 \cdot 22)^{-4} \tag{11}$$

so that the (strongly scale-selective) horizontal diffusion damps harmonics of total wavenumber 21 on a time scale τ_H = 2 days.

b) Formulation of the quasi-geostrophic model.

The QG model is a global T21 spectral model with three pressure levels in the vertical, identical to the model described in *Marshall and Molteni* (1992). The model integrates prognostic equations for QG potential vorticity (PV) at 200 hPa (level 1), 500 hPa (level 2) and 800 hPa (level 3) of the form:

$$\frac{\partial q_1}{\partial t} = -J\,(\psi_1, q_1) - D_1\,(\psi_1, \psi_2) + S_1 \tag{12a}$$

$$\frac{\partial q_2}{\partial t} = -J\,(\psi_2, q_2) - D_2\,(\psi_1, \psi_2, \psi_3) + S_2 \tag{12b}$$

$$\frac{\partial q_3}{\partial t} = -J\,(\psi_3, q_3) - D_3\,(\psi_2, \psi_3) + S_3 \tag{12c}$$

where the index i = 1, 2, 3 refers to the pressure level. PV is defined as:

$$q_1 = \nabla^2 \psi_1 - R_1^{-2} (\psi_1 - \psi_2) + f \tag{13a}$$

$$q_2 = \nabla^2 \psi_2 + R_1^{-2} (\psi_1 - \psi_2) - R_2^{-2} (\psi_2 - \psi_3) + f \tag{13b}$$

$$q_3 = \nabla^2 \psi_3 + R_2^{-2} (\psi_2 - \psi_3) + f (1 + h/H_0) \tag{13c}$$

where R_1 (=700 km) and R_2 (=450 km) are Rossby radii of deformation appropriate to the 200-500 hPa layer and the 500-800 hPa layer respectively, h is the (real) orographic height and H_0 a scale height (set to 9 km).

In Eqs. 12 D_1, D_2, D_3 are linear operators representing the effects of newtonian relaxation of temperature, linear drag on the 800 hPa wind (with drag coefficient depending on the nature of the underlying surface) and horizontal diffusion of vorticity and temperature. (These operators are described in detail in Appendix A.) The temperature relaxation has a radiative time-scale of 25 days, while the linear drag on the low-level wind has a spin-down time-scale of 3 days over the oceans, 2 to 1.5 days over land (depending on the orographic height); the horizontal diffusion, acting on the time-dependent part of the PV fields, has the same formulation as in the barotropic model.

The terms S_1, S_2 and S_3 are spatially varying sources of PV, which are necessary to obtain a realistic climatology from non-linear integrations of the model. However, they do not appear in the linearised version of the model used to compute the fastest-growing perturbations, so we do not need to define them at this stage. We shall do so in Section 6, when non-linear integrations of the QG model will be discussed.

Both the barotropic and the three-level QG model have been linearised and, for any given time-independent basic state, converted to a matrix operating on a state vector of non-null spherical harmonic coefficients (the degrees of freedom are 483 and 1449 for the two models respectively). From such a matrix L, the resolvent for a 6-hour integration period has been computed as the exponential of L using a Taylor expansion, and the resolvents for 12 hours, 24 hours, 48 hours etc. have been computed as powers of the 6-hour resolvent. Finally, the adjoint of the resolvent has been computed by taking the transpose of the resolvent matrix and multiplying its rows and columns by weights appropriate to the energy inner product definition.

4. INSTABILITY OF THE CLIMATOLOGICAL BASIC STATE.

a) barotropic instability

Fig. 1 shows the 300 hPa streamfunction constructed from 6 years of ECMWF January-February analyses. Relative to this basic state, the amplification factor of the most unstable barotropic normal mode, and the

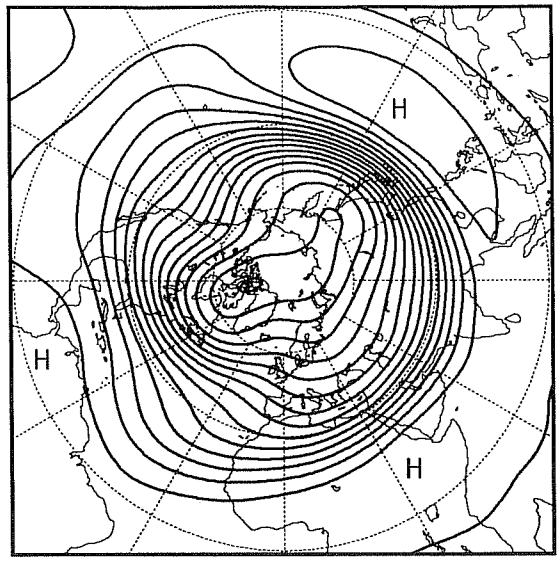

Fig. 1 Climatological 300 hPa streamfunction based on January-February mean over 6 winters from ECMWF analyses. Contour interval 10^7 m^2/s.

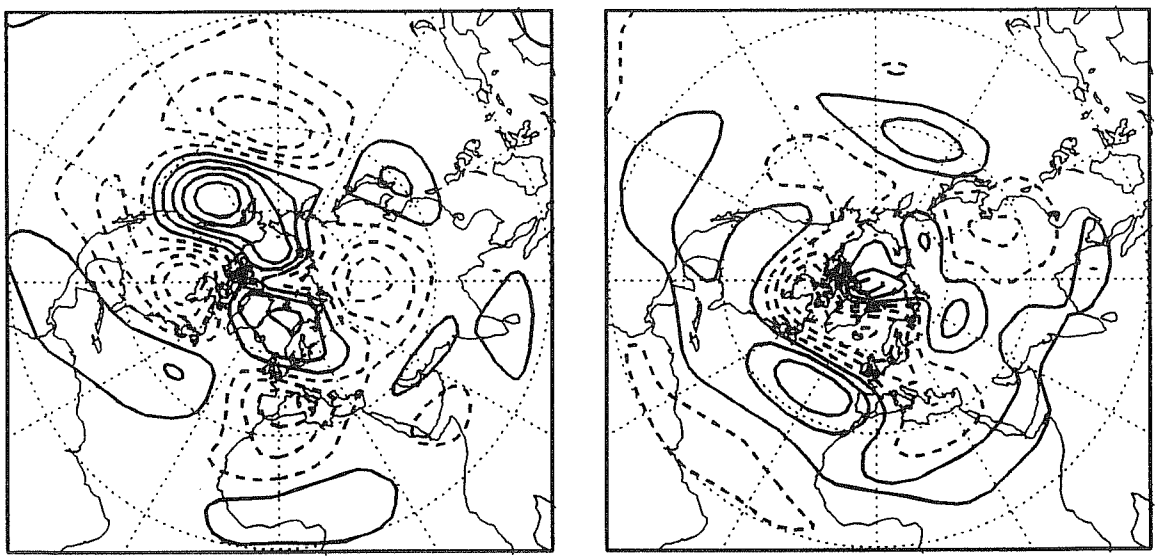

Fig. 2 Streamfunction of the most unstable normal mode for the climatological basic state in Fig. 1. Contour interval arbitrary, negative values dashed.

amplification factor of the optimal barotropic SV (i.e. the value of I in Eq. 8)) are shown in Table 1 (first 2 columns) as a function of optimisation time.

Starting with unit amplitude the most unstable normal mode is slowly decaying with time. This is related to the fact that the dissipation in the barotropic model renders the mode almost neutral. By contrast, the optimal SVs exhibit substantial growth at least up to the 16 day period shown. (The last two columns of the table are for the baroclinic case to be discussed below).

The structure of the most unstable normal mode, shown in Fig. 2, is comparable with that in *Simmons et al.* (1983). The two phase quadrature components of the mode are characterised by large scale disturbances with some correspondence to observed teleconnection patterns in the atmosphere (cf *Ferranti et al.*, 1990). In our model, which adopts a different climatological basic state from the one used in *Simmons et al.*, the mode has a period of 22 days.

By definition the disturbance pattern shown in Fig. 2 describes the fastest normal mode amplification for all integration periods. For the optimal SV calculations, a different eigenvector is associated with each optimisation period. The columns of Table 2 show the time evolution of the (wind) amplitude for each SV that is optimal for days 1/2, 1, 2, 4 and 8 respectively. The diagonal entries correspond to values shown in Table 1. It is interesting to note that a barotropic SV designed to be optimal over a given time period, can be quite suboptimal for any other time period. Take for example the SVs at day 2; from the third row of Table 2, the amplification of the 12hr SV is only 58% of optimal amplification (this behaviour will be contrasted in section 3b with that of a baroclinic atmosphere).

Fig. 3 shows the barotropic SVs, optimised for days 1/2, 2 and 8, together with their evolution at the same times. The first column shows the initial structure of the three optimal SVs. For the 12hr SV, the structure is highly localised (compared with the normal mode in Fig. 2), with an amplitude maximum over the subtropical western Pacific extending down into the tropics. The horizontal phase gradient associated with the disturbance indicates that it is gaining energy from the mean flow by barotropic energy conversion. There is clearly some correlation between the initial structure of the 12-hour and 2 day SVs, though the latter is less localised, with amplitude over much of the Asian landmass. The localisation of the initial disturbance is less apparent for 8-day SV.

The evolution of each SV is shown by a row of Fig. 3. For the 12 hour SV, the localised perturbation has dispersed downstream as far as the dateline within 12 hours. By day 2, the leading edge has reached the west coast of north America, and by day 8 it has begun to be damped significantly as it propagates over the north

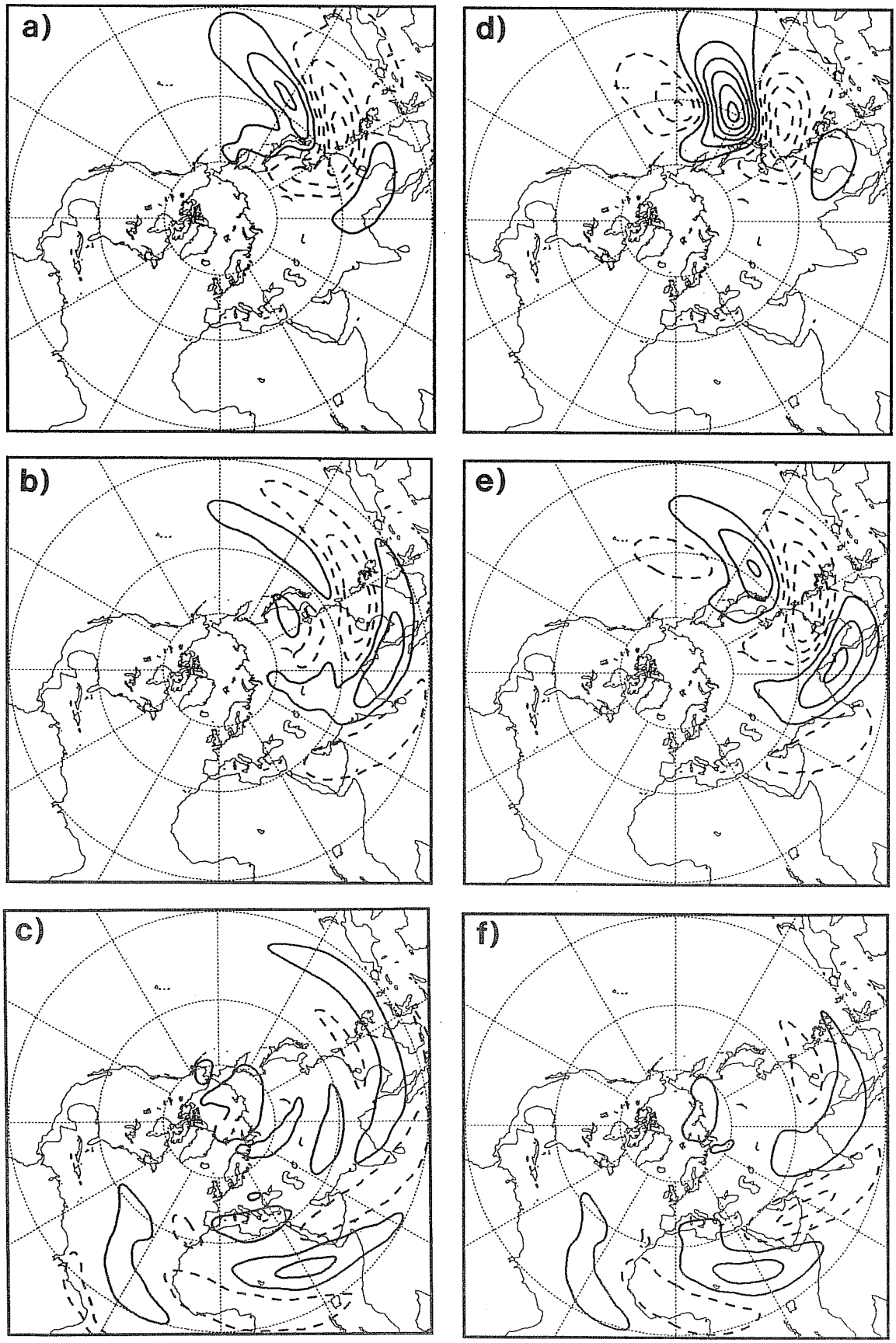

Fig. 3 a-c): streamfunction of the 12-hour (a), 2-day (b) and 8-day (c) optimal barotropic SVs at day 0, with a rms wind norm of 1 m/s; contour interval $1.5 \cdot 10^6$ m^2/s; d-f): time evolution of the SVs shown in panels a-c respectively, after 12 hours of linear integration; contour interval $2. \cdot 10^6$ m^2/s; g-i): as in d-f) respectively, but after 2 days; contour interval $3. \cdot 10^6$ m^2/s; j-l): as in d-f) respectively, but after 8 days; contour interval $3. \cdot 10^6$ m^2/s.

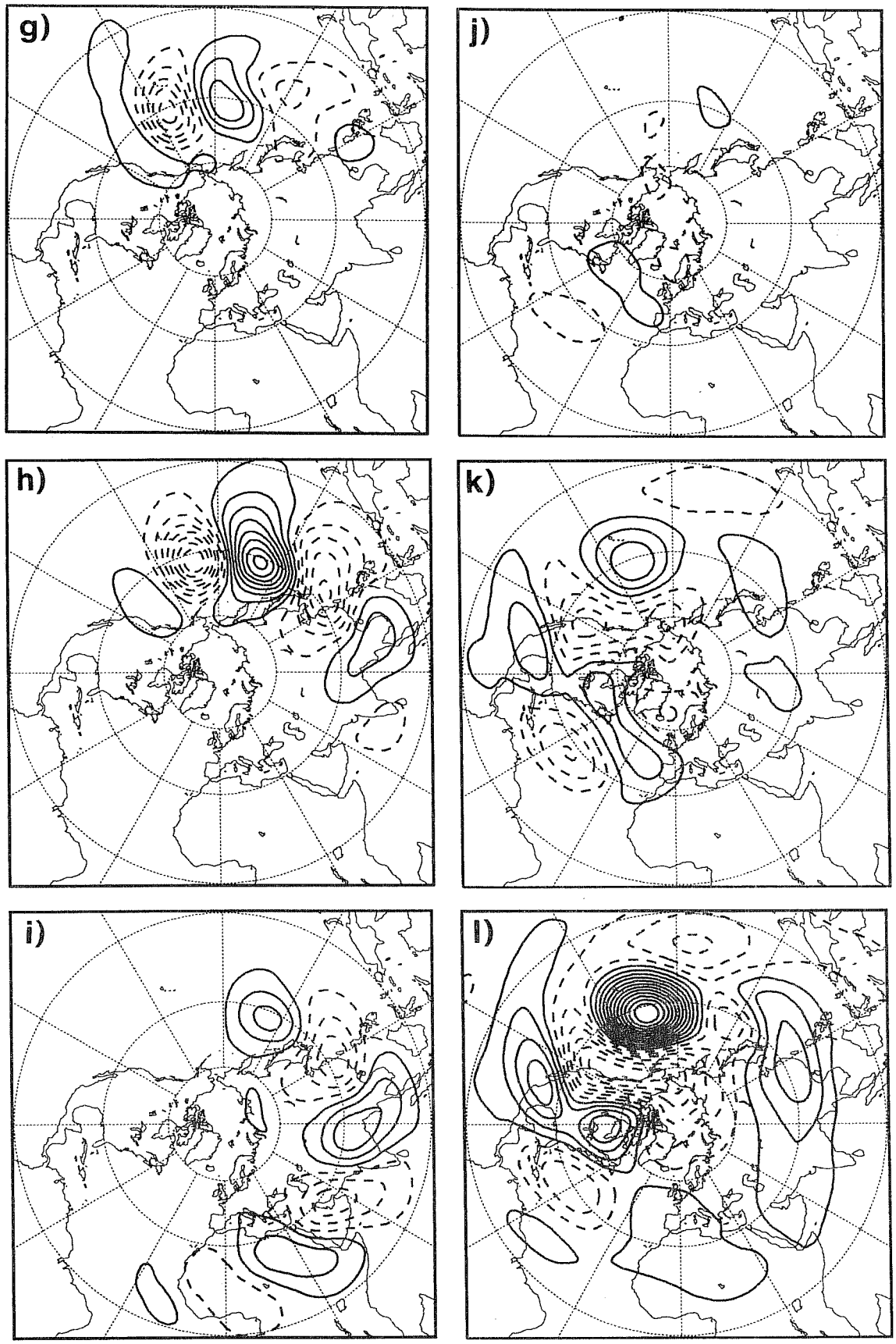

Fig. 3 continued.

Atlantic. The structure and position of the day 2 SV is fairly similar to the 12 hour SV at day 2, though the day 2 SV has significantly more amplitude at day 8. The structure of the day 8 SV is quite similar to that of the day 2 SV at day 8, but, by definition, with higher amplitude.

It can be seen from Fig. 3 that the structure of the day 8 SV begins to resemble one phase of the normal mode as it evolves to optimisation time. As discussed in section 2 this is characteristic of the asymptotic behaviour of the optimal SVs with time-independent basic states, and indicates that significant convergence to this asymptotic state has occurred by 8 days.

b) baroclinic instability

We have repeated the calculations outlined above using the 3-level QG model described in section 2. The basic state is again taken from 6 years of ECMWF January-February analyses, and is shown in Fig. 4 at the three levels of the model.

The growth of the fastest normal mode and the corresponding optimal SV are shown in the last two columns of Table 1. Unlike the barotropic case, the most unstable baroclinic normal mode amplifies with time. However, as in the barotropic model, the optimal SVs have significantly larger growth rates throughout the range of time intervals studied (about an order of magnitude larger at day 4).

Comparing the barotropic and baroclinic growth rates, it is interesting to note that the optimal barotropic SVs have larger amplification rates than the fastest growing baroclinic normal mode up to an 8 day time interval. Moreover, between the barotropic and baroclinic SVs, the difference in amplitude at day 2 is just over a factor of 2. If, as *Farrell* has conjectured, synoptic disturbances are associated with excitation of these optimal SVs by stochastic noise, barotropic energy conversions for the synoptic scales cannot be ignored.

The structure of the most unstable normal mode, in two phase-quadrature components, is shown in Fig. 5 at the three levels of the QG model. The structure of the disturbance shows the familiar westward tilt with height, indicating that the mode can gain energy from the mean flow by baroclinic processes (though it loses energy to the mean flow by barotropic conversions, in the opposite sense to the barotropic SVs).

The amplification rates for the baroclinic SVs at different time ranges is shown in Table 3, in a form similar to that discussed in Table 2 for the barotropic SVs. There are some interesting comparisons with the barotropic case. For example, the amplification at day 2 of a 12-hour SV is 5.4, compared with 7.4 for an day-2 SV evaluated at day 2. Therefore, the baroclinc SVs calculated over a short time interval are less sub-optimal at longer ranges than the equivalent barotropic SVs. This result is significant in formulating a strategy for choosing QG SVs as initial perturbations in ensemble forecasting (see MMP): it suggests that the

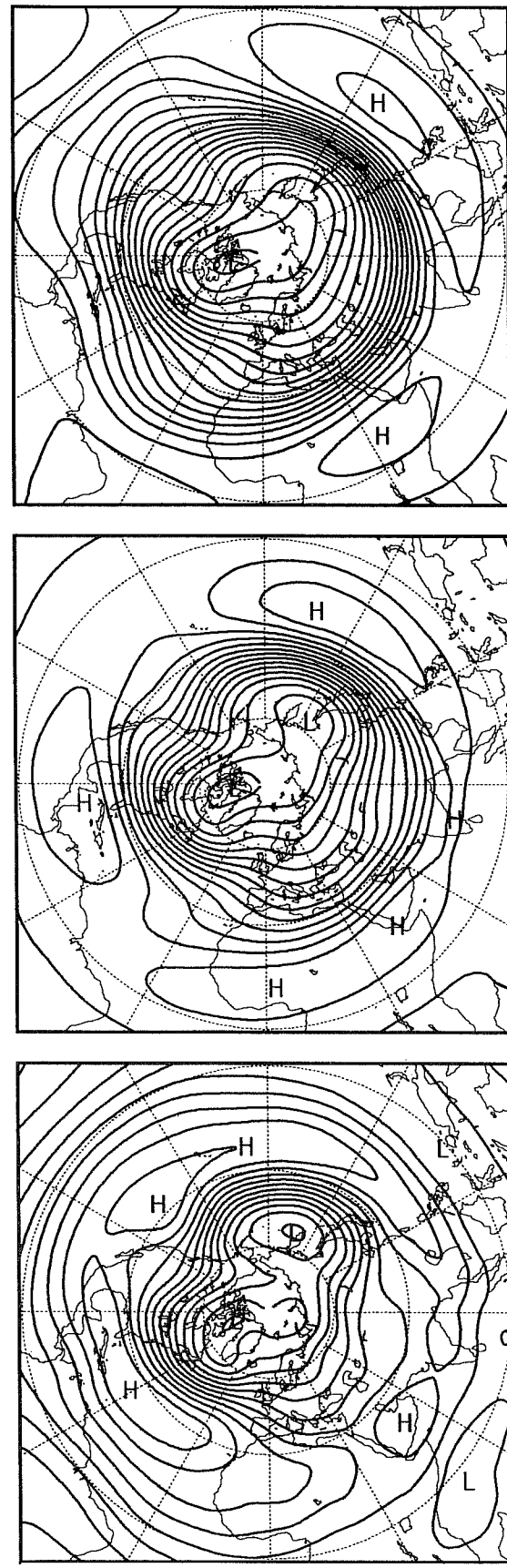

Fig. 4 Climatological streamfunction based on January-February mean over 6 winters from ECMWF analyses. Top 200 hPa, middle 500 hPa, bottom 800 hPa. Contour intervals 10, 6 and $3 \cdot 10^6$ m^2/s respectively.

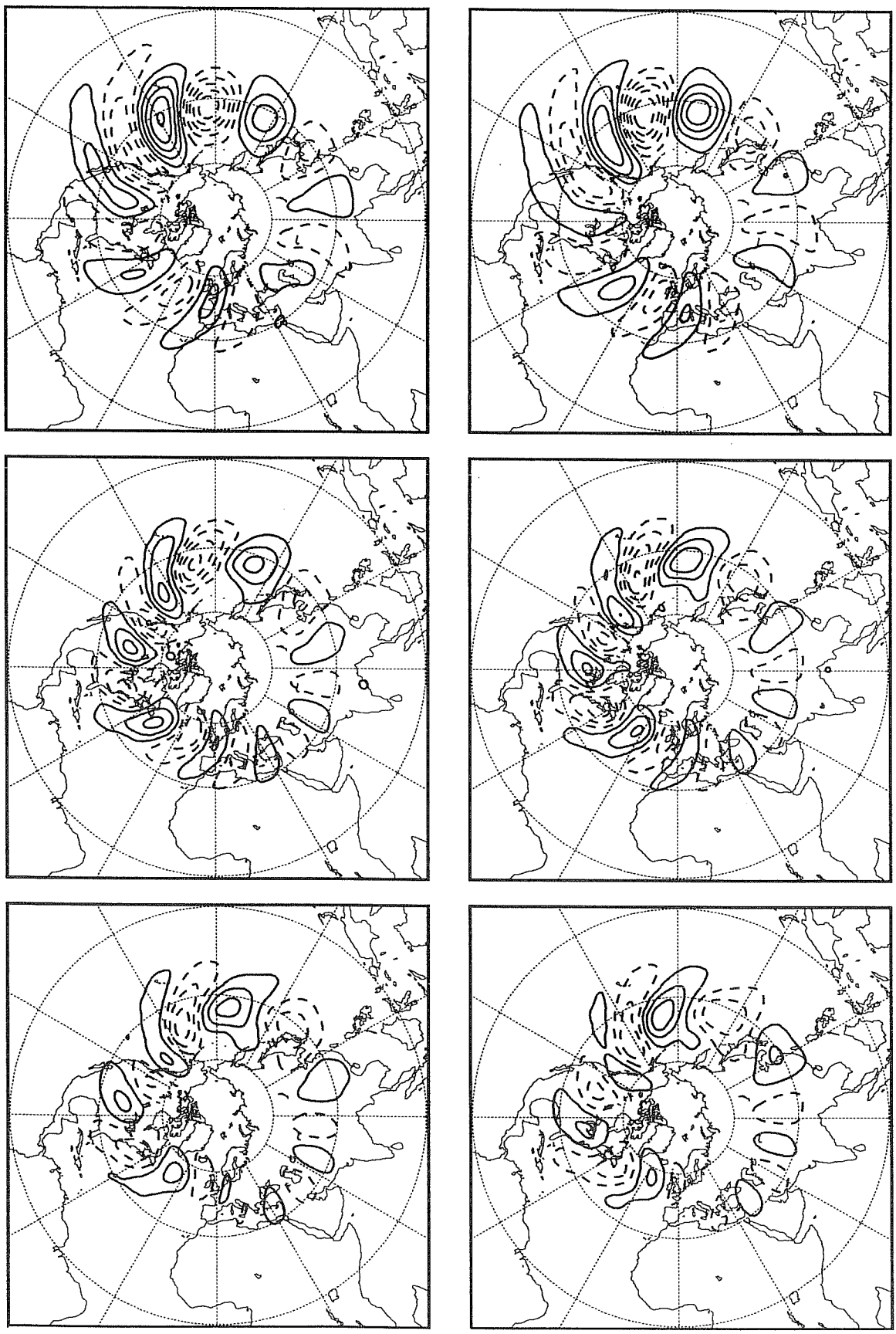

Fig. 5 Fastest growing baroclinic normal mode for the basic state in Fig. 4. Top 200 hPa, middle 500 hPa, bottom 800 hPa.

energy growth obtained from very-short-range optimisation may not be much different to that obtained by optimising at the limit of applicability of linear error growth (about 2 days). Conversely, as Tables 2 and 3 show, baroclinic SVs optimised over relatively long time intervals (e.g. 8 days) and evaluated over shorter time intervals (e.g. 2 days) are much more suboptimal than in the barotropic case, though this result is of less practical importance.

In order to understand these differences more clearly, Figs. 6-8 shows the 12 hours, 2 days and 8 days baroclinic SVs respectively, evaluated at the initial time, and at 12 hours, 2 days and 8 days. Each column of these figures gives the SV at the three levels of the QG model.

The initial structure of the baroclinic SV optimised for 12 hours has interesting similarities with the barotropic SV at the barotropic level (cf Fig. 3). In particular the baroclinic SV shows the horizontal phase tilt characteristic of energy conversion from mean flow to the disturbance. Unlike the barotropic SV, however, the baroclinic SV is much more localised in the meridional direction, with little amplitude in the tropics, and with a maximum closer to the jet core. Moreover, the vertical structure shows clear westward tilt with height similar to the normal mode. Therefore, in the 3-level model that the optimal SV grows initially as a result of both baroclinic and barotropic energy conversions.

The third and fourth columns of Fig. 6 show the evolution of the optimal 12 hour SV at days 2 and 8 respectively. At day 2 the initial disturbance has dispersed downstream as far as the east Pacific. It is interesting to note that both the barotropic and baroclinic phase tilts are now much reduced over their initial values, consistent with the fact that the main energy growth has already occurred. By day 8 the disturbance has dispersed downstream as far as the north Atlantic.

Fig. 7 shows the initial structure and evolution of the 2 day SV. As with the barotropic mode, the initial structure of this SV is located over the Asian land mass; the amplitude is predominantly located in the bottom two layers of the model. As with the 12-hour SV there are significant phase tilts in the horizontal and vertical. By day 2, the SV has dispersed downstream and is fairly well correlated with the pattern of the 12-hour SV at day 2 (cf discussion above). Note that the amplitude of the upper tropospheric level has grown considerably over the first two days. Again, the disturbance has dispersed as far as the north Atlantic by day 8.

The initial structure of the SV optimised for day 8 is not well localised in the zonal direction, and has the appearance of an extended wavetrain over Africa, Europe and Asia (Fig. 8). By day 8, the day-8 SV has a fairly hemispheric pattern with some correspondence, particularly over the north Pacific, to the first normal mode shown above.

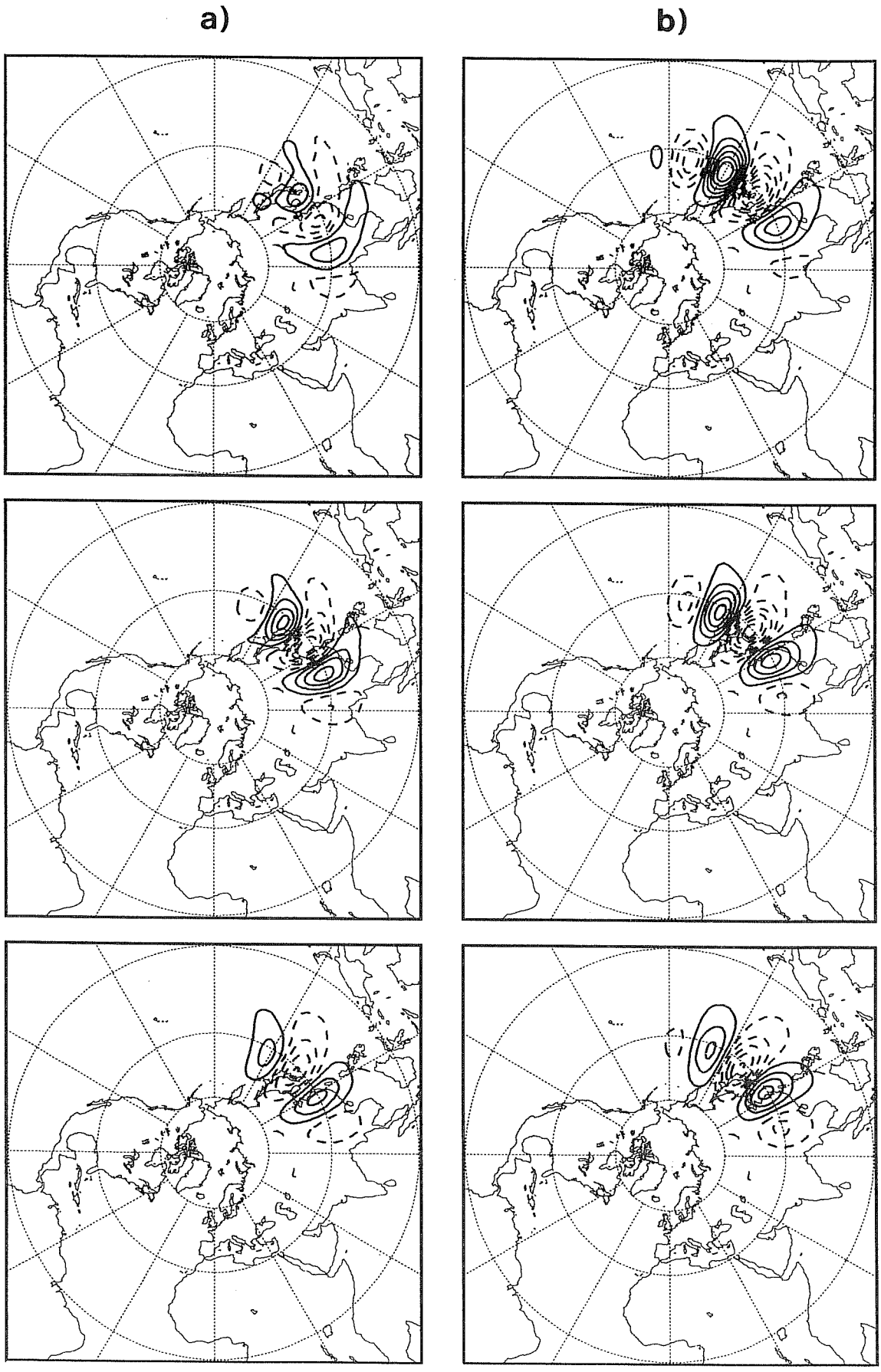

Fig. 6 Fastest growing baroclinic 12-hour SV evaluated at: day 0 (column a; contour int. = $1.5 \cdot 10^6$ m^2/s), day 1/2 (column b, contour int. = $2.5 \cdot 10^6$ m^2/s), day 2 (column c; contour int. = $7. \cdot 10^6$ m^2/s), day 8 (column d, contour int. = $15. \cdot 10^6$ m^2/s). Top row 200 hPa, middle row 500 hPa, bottom row 800 hPa.

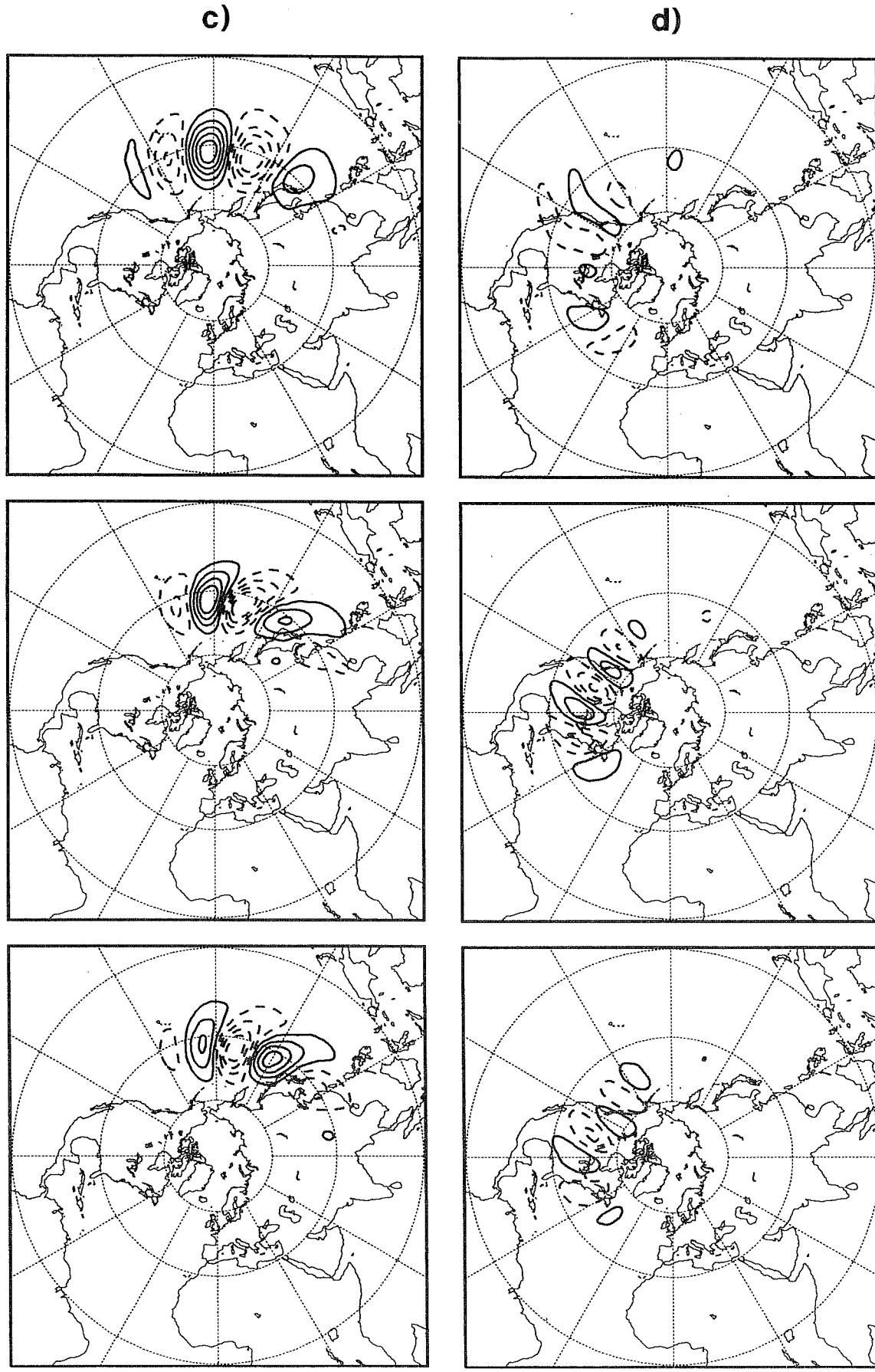

Fig. 6 continued.

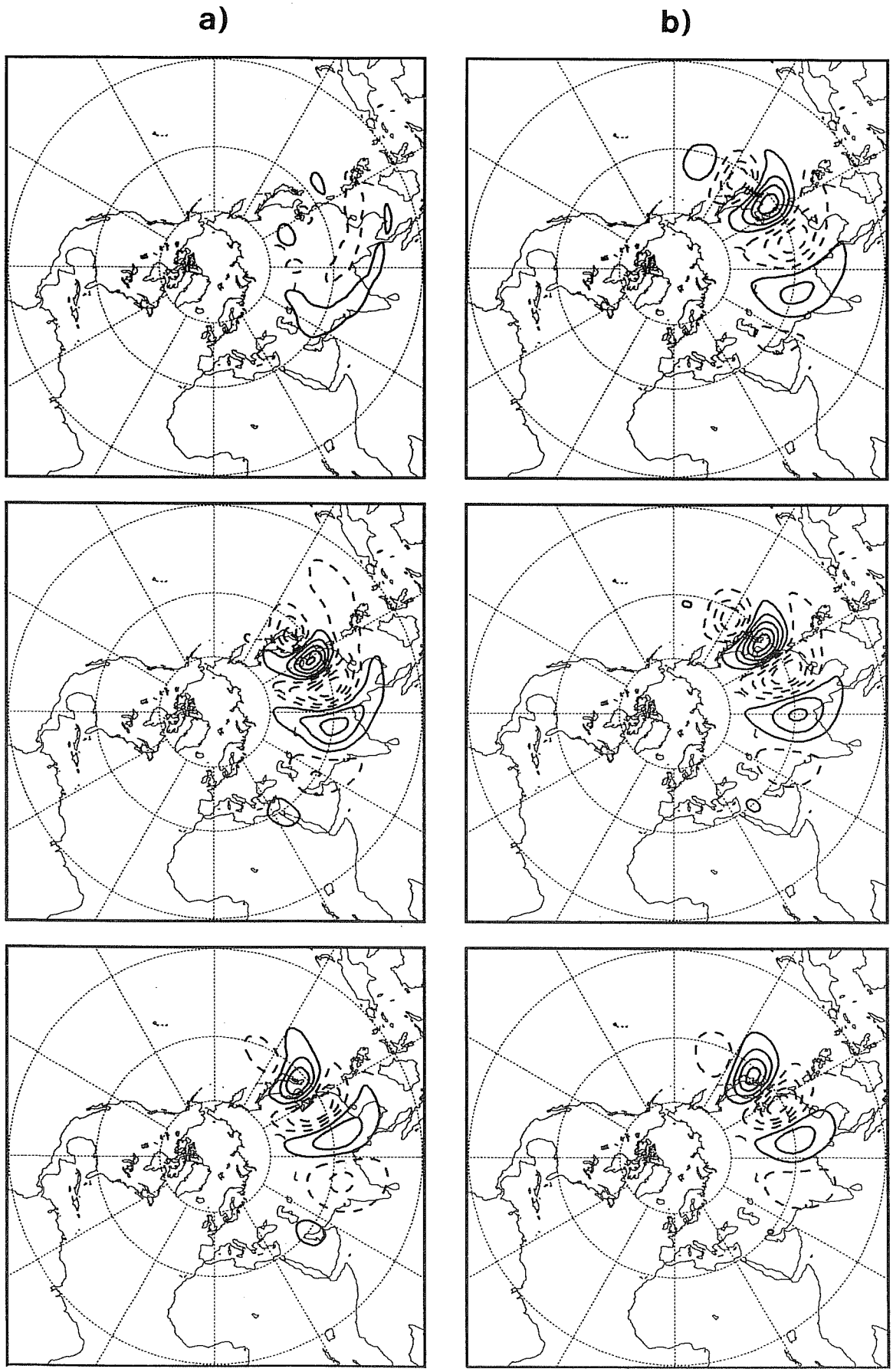

Fig. 7 As Fig. 6 but for fastest growing day-2 SV.

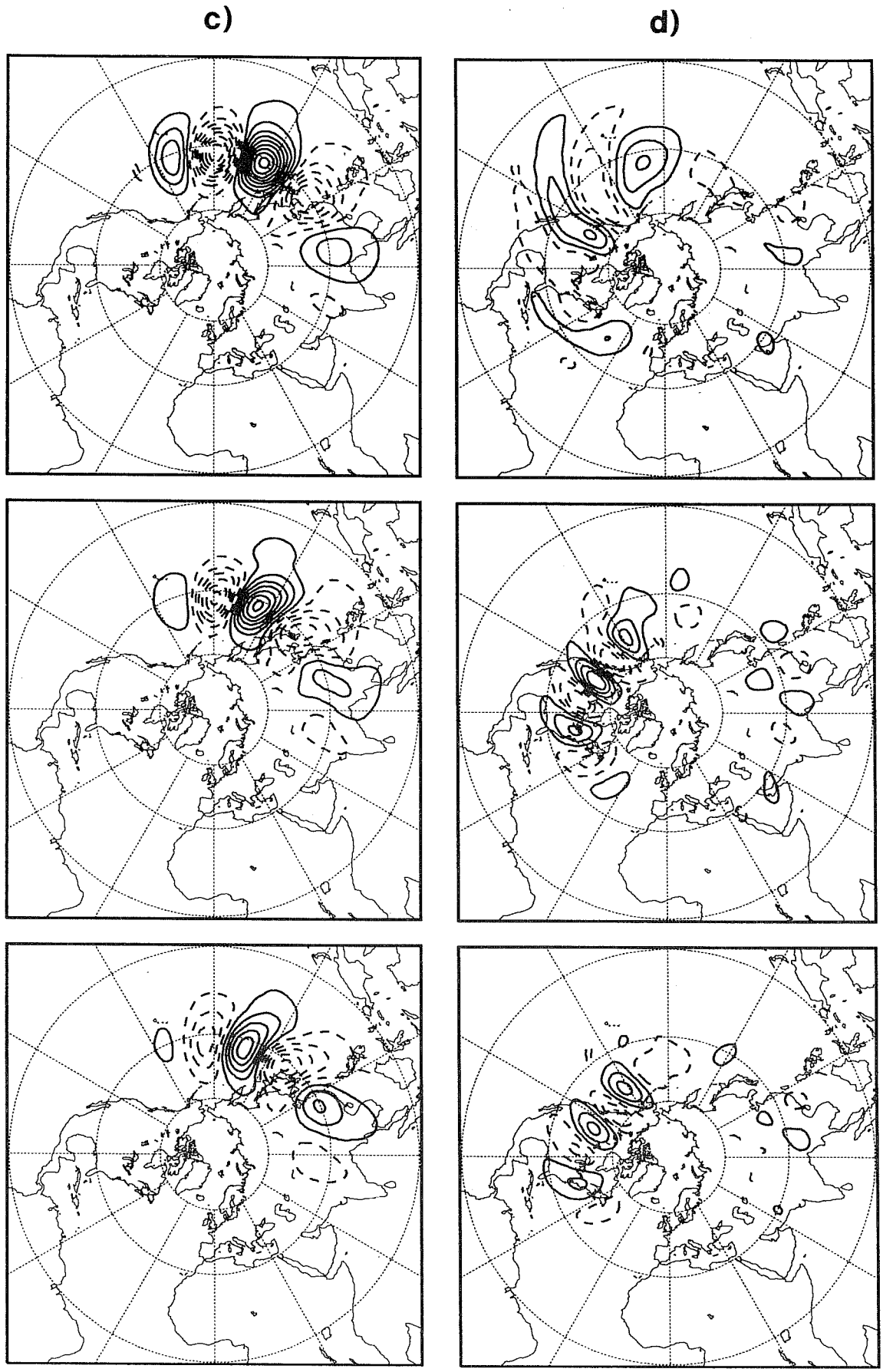

Fig. 7 continued.

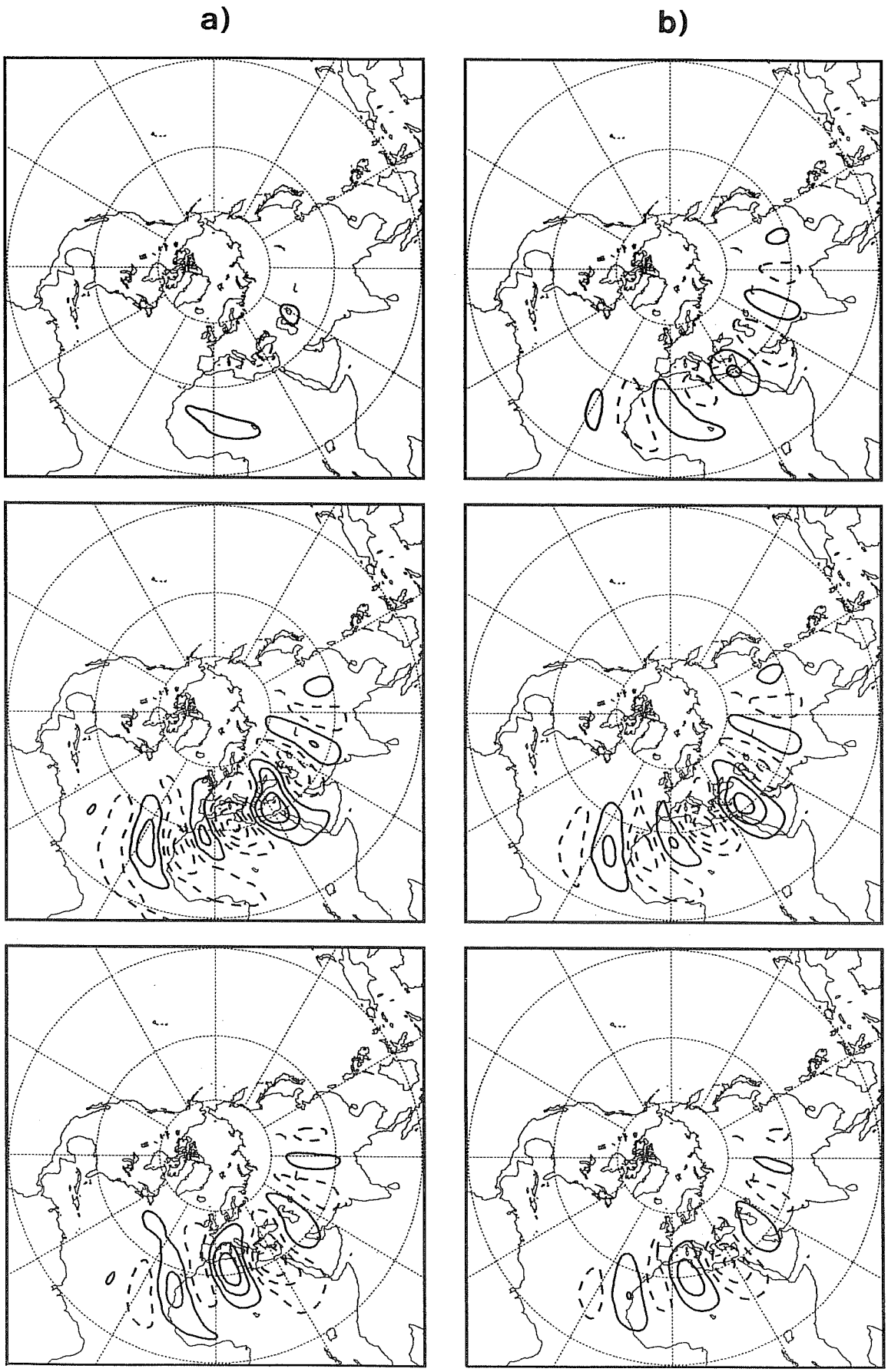

Fig. 8 As Fig. 6 but for fastest growing day-8 SV.

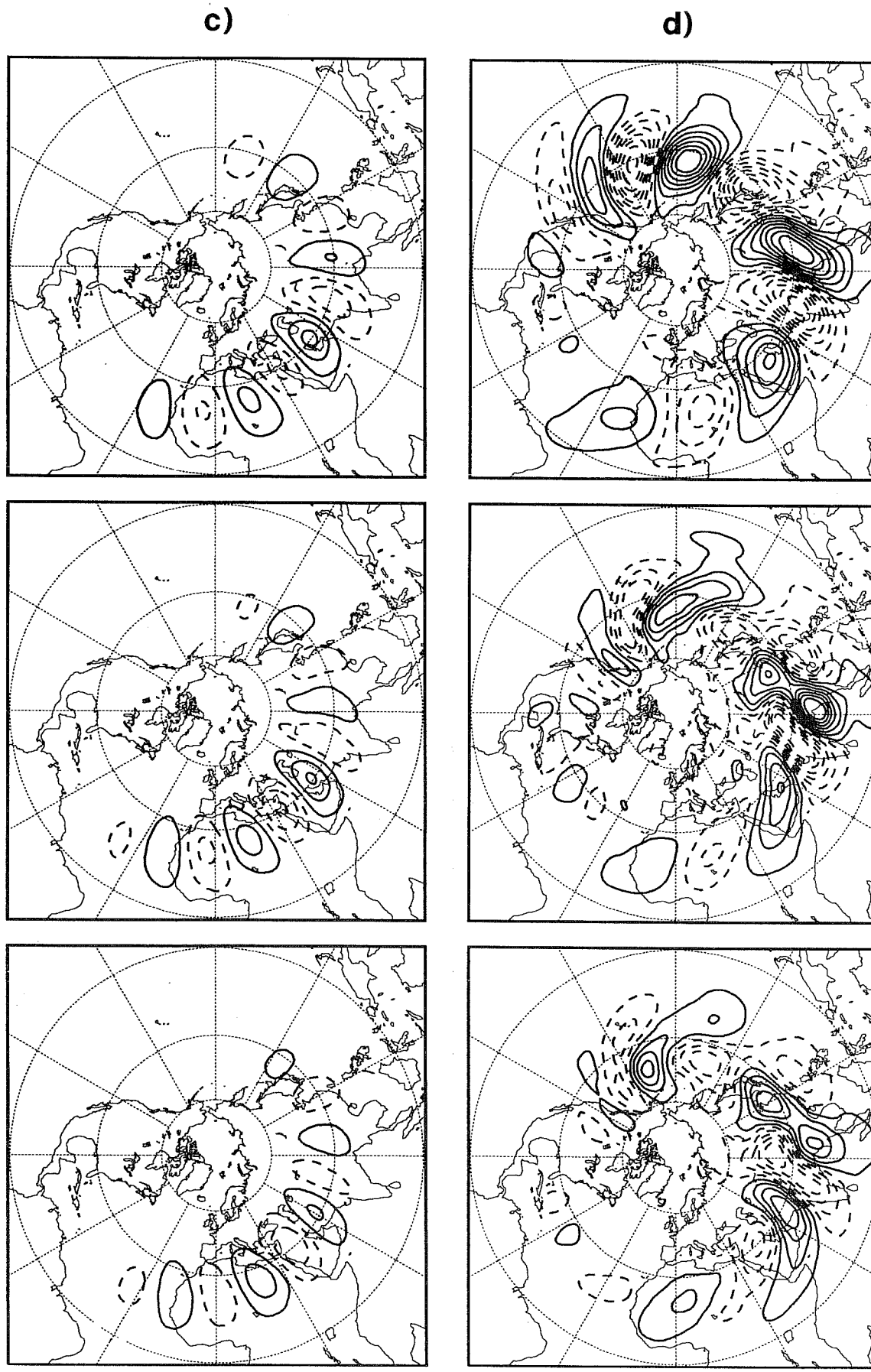

Fig. 8 continued.

For brevity we shall not show here other members of the spectrum of the SVs; however, some of these are discussed in the companion paper by MMP.

5. INSTABILITY OF REGIME CENTROIDS

The existence of regimes in the winter northern flow appears to have been confirmed by a number of independent studies (*Mo and Ghil*, 1988, *Molteni et al.*, 1990, *Cheng and Wallace*, 1991). From a theoretical point of view the existence of such regimes can be viewed as a consequence of the internal nonlinear dynamics of the midlatitude flow, as suggested by highly truncated models.

Many of the dominant regimes of the northern winter circulation have a marked projection onto the Pacific/North American (PNA) teleconnection pattern (*Wallace and Gutzler*, 1981). In particular, two of *Molteni et al.'s* (1990) regime centroids, have significant projection onto opposite phases of the PNA pattern and are shown in Fig. 9 as full fields of 500 hPa streamfunction (the method used to construct global, 3-dimensional streamfunction fields corresponding to the cluster centroids is described in Appendix B). By convention, the centroid in Fig. 9a, equivalent to cluster 2 of *Molteni et al.*, has positive PNA index (corresponding to a strong zonal flow over the eastern Pacific, and an enhanced ridge over the Rocky Mountains); the centroid in Fig. 9b, cluster 5 of *Molteni et al.*, has negative PNA index, corresponding to a ridge over the eastern Pacific. (Two of *Molteni et al.'s* regime centroids have negative PNA index; of these, the one shown in Fig. 9b has a more negative index.)

Evidence of variations in the instability characteristics of positive and negative PNA states was discussed in *Palmer* (1988), who found that the growth of initial perturbations in a linearised barotropic model depended strongly on the signed amplitude of the PNA index of the basic state flow. It was noted that the difference in these growth rates could not be explained in terms of differences in the normal mode growth associated with the basic states. *Zhang* (1988) analysed positive and negative PNA flows in terms of the normalised scalar product between the fastest growing normal mode and its adjoint. Clearly the value of this scalar product is related to the degree the resolvent operator fails to be self adjoint.

Palmer (1988) also found that the medium-range forecast skill of the ECMWF model depended on the signed amplitude of the forecast PNA pattern. *Molteni and Tibaldi* (1990) took this analysis further by studying the skill of the operational model associated with the clusters analysed by *Molteni et al.* (1990); they found that the failure to predict the correct cluster tends to lead to a larger medium-range forecast error in those cases when the atmosphere moves to (or persists in) a negative PNA state.

Table 4 shows the growth rates of the fastest growing normal modes and the optimal SVs for the cluster 2 and cluster 5 flow in the barotropic model. For the most unstable normal mode (which nb is stationary in

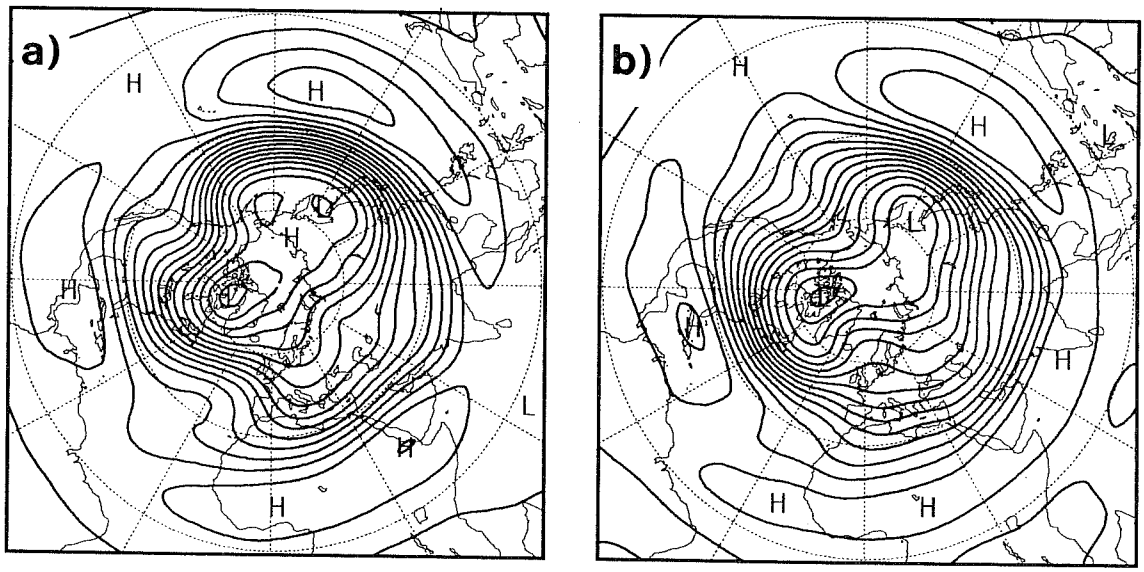

Fig. 9 500 hPa streamfunction associated with cluster centroid numbers 2 (a) and 5 (b) of *Molteni et al.* (1990). Contour interval $6.\cdot 10^6$ m^2/s.

both cases), there is little difference in growth rates for the two basic states. On the other hand, the optimal SVs show significant difference in growth rates. In particular, by day 8, the amplitude of the optimal SV for the cluster 2 flow is almost a factor of 2 smaller than that of the cluster 5 flow.

Fig. 10 shows the evolution in the barotropic model of the 2-day SV for cluster 2 and cluster 5, evaluated at days 2,4 and 8. There is not a great deal of difference between the initial perturbations (not shown); both are close to the optimal 2-day SV for climatology shown in Fig. 3. By day 2 the cluster 2 SV has dispersed further downstream to the north-east Pacific - though there is little apparent difference in the amplitude of the cluster 2 and cluster 5 perturbations. Interestingly, by day 4 the cluster 2 optimal SV propagates further downstream over north America, whilst the cluster 5 SV becomes stationary and grows in situ over the north-east Pacific. By day 8 the SVs have begun to project onto the most unstable normal modes of these basic states (not shown), with the cluster 5 perturbation having larger amplitude.

SVs optimised for day 8 are shown in Fig. 11 at day 8 only. The resulting disturbances are not dissimilar to the evolution at day 8 of the day-2 SVs shown above though with larger amplitude. As above, the cluster 5 flow has a larger disturbance amplitude than the cluster 2 flow.

The normal modes and SVs of cluster 2 and 5 flow have also been studied using the three-level QG model; their maximum growth rates are compared in Table 5. (For brevity the 3-dimensional fields corresponding to the cluster centroids are not shown here.) As with the barotropic model, the difference between the normal mode growth rates is small, and there is little difference in amplitudes up to day 8. For the optimal SVs, one can note that the cluster 2 basic state has a larger growth than cluster 5 up to day 4, whilst beyond this range cluster 5 has the larger amplification. However, these differences are much smaller than in the barotropic case: at day 8, the amplification factor of the optimal SV is 28.8 for cluster 5, against a value of 25.7 for cluster 2.

Are the barotropic or the baroclinic results in closer agreement with forecast errors observed during the two regimes? *Molteni and Tibaldi* (1990) computed hemispheric mean-square errors of day 6-to-10 ECMWF forecasts of 500 hPa height for a seven-winter period, and estimated the average values of such errors depending on the observed regime and on whether the regime was correctly or incorrectly predicted (see their Fig. 3). They showed that the mean square error in cluster 5 was only slightly larger than that in cluster 2 when the two regimes were correctly predicted, but significantly larger when the regime was incorrectly predicted. They also showed that the performance of the model was better in persistence cases than in transition cases, a result also found for the prediction error of other NWP centres (see for example *Chen*, 1989). Since we have kept our basic states fixed to one cluster centroid, the figures just discussed are clearly more relevant to cases of regime persistence than to cases of regimes transition. If we assume that the

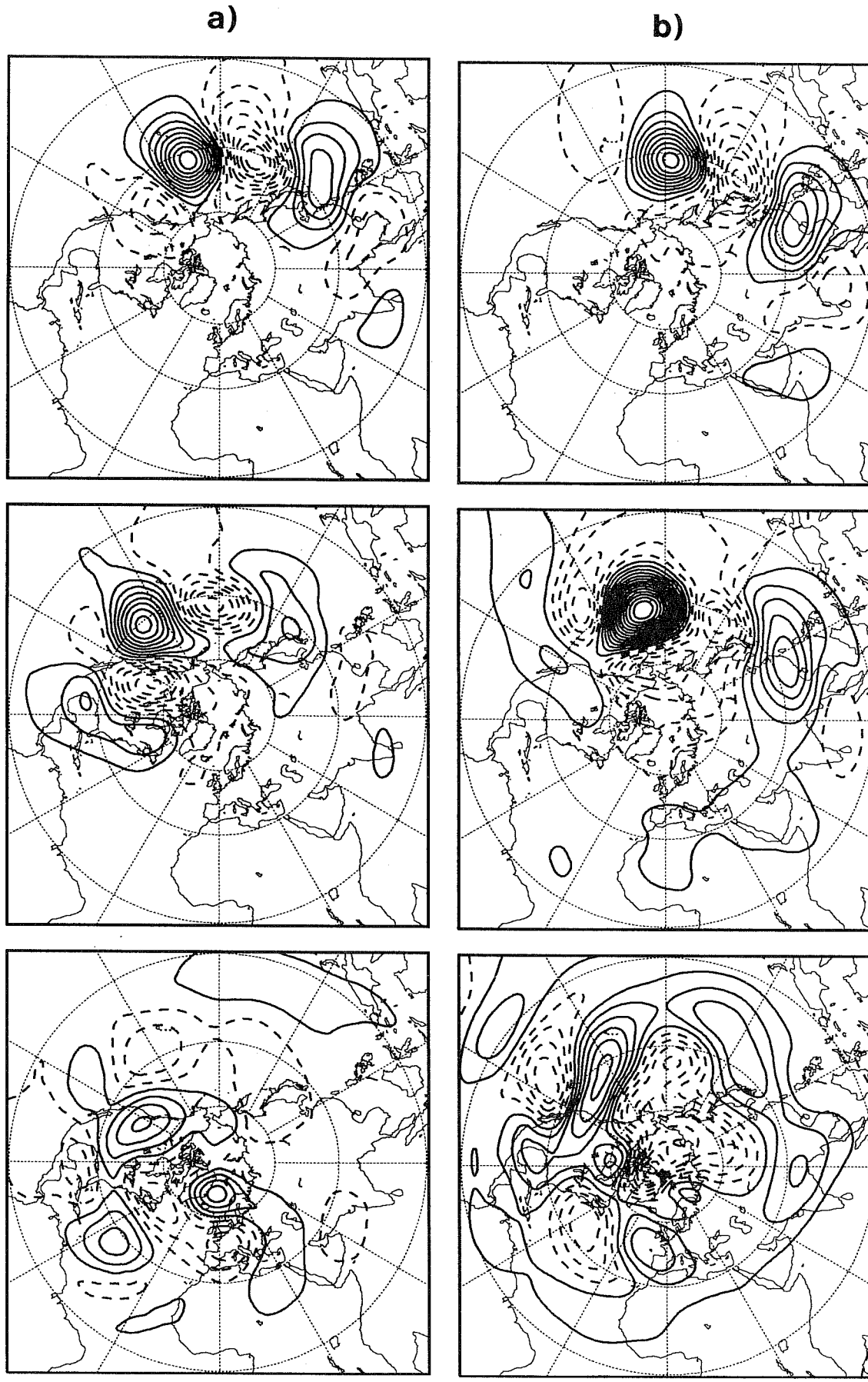

Fig. 10 Evolution of fastest growing barotropic day-2 SV at days 2 (top), 4 (centre) and 8 (bottom) for cluster 2 (column a), and cluster 5 (column b). Contour interval $3.\cdot 10^6$ m^2/s.

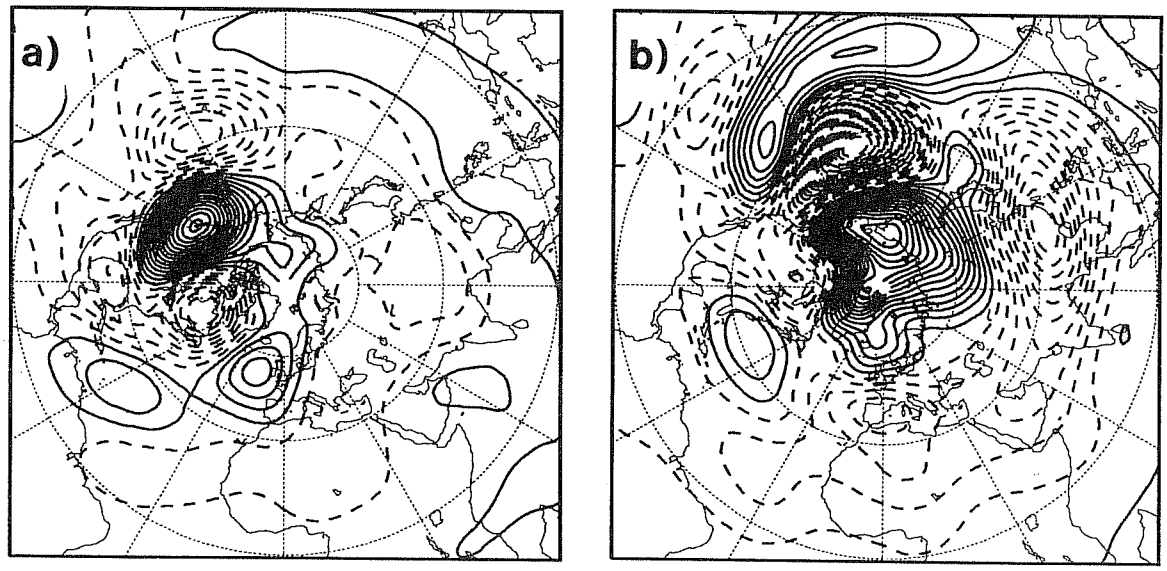

Fig. 11 Optimal barotropic day-8 SV at day 8 for a) cluster 2 and b) cluster 5. Contour interval $3.\cdot 10^6$ m^2/s.

amplification factors with fixed basic states should be compared with the forecast errors in regime-persistence cases (when the model is likely to predict correctly the regime itself), then we find that the ratio of the hemispheric rms errors in cluster 2 and cluster 5 (70 m and 77 m respectively, as deduced from *Molteni and Tibaldi*) is closer to the ratio of the baroclinic than to the ratio of the barotropic amplification factors.

On the other hand, even in cases of regime persistence, error growth and predictability on a regional scale can be quite different between clusters 2 and 5, due to the different phase of the large-scale waves. In order to address these problems, we show in Fig. 12-13 the growth of the baroclinic SVs at the upper (200 hPa) level only, for the day-2 and day-8 optimal SVs, in the same format as for the barotropic model (cf Figs. 10 and 11). For the day-2 SVs, there is little difference in the initial structure of the perturbations (not shown), which have relatively small amplitude at the upper level. By day 2, as with the barotropic model, the cluster 2 SV has dispersed further downstream and, has a little more amplitude over the north Pacific. At day 4 and 8, the baroclinic day-2 SVs have a qualitatively similar behaviour to their barotropic counterparts; in particular, the cluster 2 SV continues to propagate eastward, whilst the cluster 5 SV amplifies in situ over the north east Pacific.

Fig. 13 shows the baroclinic day-8 SVs at the day 8 optimisation time. The result here is qualitatively different to the results above. For the cluster 2 centroid, the SV has most amplitude over the Indian subcontinent; by contrast, for the cluster 5 centroid, the perturbation amplitude maximum is located near the date line. In particular, evaluated over the PNA region, the optimal baroclinic SV has a much larger amplitude for negative PNA flow than for positive PNA flow, in agreement with the regional error studies described in *Palmer* (1988) and *Palmer and Tibaldi* (1988).

It should be noted, however, that none of the SV perturbations shows a strong projection on zonal wavenumbers 1 to 4, which characterise large-scale regimes. The cluster centroids used as basic states are smooth fields, and contain only large-scale waves. It appears that a synoptic-scale perturbation evolving linearly on such basic states is unable to produce any significant eddy-eddy interaction which can transfer energy from the synoptic to the planetary-scale waves, and consequently cause a large-scale regime transition. This argument supports our previous statement that linear baroclinic instability of a time-invariant cluster centroid can better explain errors in regime persistence than in regime transition cases.

The results above suggest that, in order to find baroclinic instability indices which are related to the amplitude of forecast errors in cases of regime transitions, one must follow the evolution of the perturbations when they are superimposed on a time-evolving basic state (or at least on a constant basic states retaining some synoptic-scale eddies, with which the perturbation eddies can interact). We shall do so in the following sections, analysing two particular realisations of the cluster 2 and cluster 5 regimes, in order to understand

Fig. 12 As in Fig. 10 but for the optimal baroclinic day-2 SV of the cluster 2 and cluster 5 basic states. 200 hPa streamfunction only. Contour intervals 7., 10. and $15 \cdot 10^6$ m^2/s at days 2, 4, and 8 respectively.

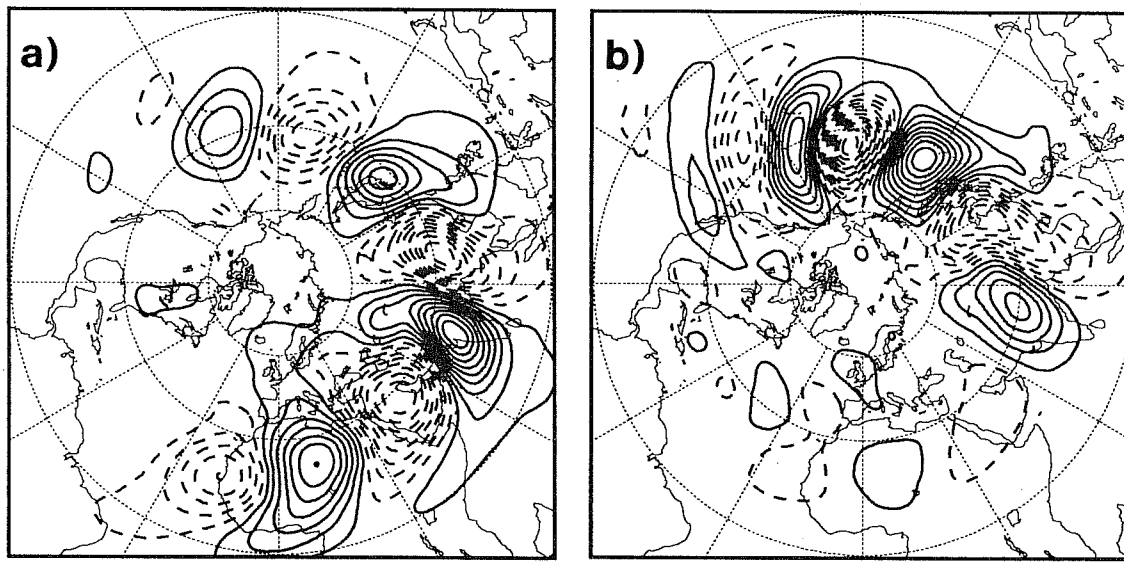

Fig. 13 As in Fig. 11 but for the optimal baroclinic day-8 SV of the cluster 2 and cluster 5 basic states. 200 hPa streamfunction only. Contour interval $15.\cdot 10^6$ m^2/s.

more completely what features of the basic state flows contribute principally to the structure and growth rates of the SVs.

6. INSTABILITY FOR TWO REALISATIONS OF CLUSTERS 2 AND 5

In this section, we discuss the finite-time instability of basic state flows which can be considered realisations of the cluster 2 and 5 composites analysed above. These case studies are investigated further in MMP, where ensemble forecasts made with the ECMWF model will be discussed.

The case studies cover two ten-day periods starting from 2 December 1988 (for the positive-PNA cluster 2) and 27 January 1989 (for the negative-PNA cluster 5), which were characterised by very different skill of the operational ECMWF forecast. The medium-range error of 500 hPa height over the northern hemisphere was much lower in the first than in the second period; the latter case is a typical example of a failure to predict a cluster-5, large-amplitude anomaly in the medium range. As reported in MMP, integrations of a recent T63 version of the ECMWF model, started from these initial dates, showed a very similar behaviour to the operational forecasts.

The evolution of the observed large scale flow in the two periods is illustrated by Fig. 14. Panels a, b show the 5-day mean analysis of 500 hPa streamfunction averaged around 2 December 1988 and 27 January 1989 respectively, while panels c, d show 5-day means of the same field centred 8 days after the initial dates. The different sign of the PNA index is already evident in the initial 5-day mean; however, the similarity with the cluster centroids shown in Fig. 9 becomes more evident eight days later: the planetary waves amplify in the Euro-Atlantic sector in the first case, in the Pacific sector (leading to a block) in the second case. The large error of the operational ECMWF forecast in the second case arose from its failure to reproduce the transition to a blocked state with large wave amplitude in the Pacific.

Transition to blocking is a problem of both theoretical interest and practical importance for weather prediction. We wanted to investigate not only if the growth of the optimal SV could explain the difference in the ECMWF forecast error, but also if the optimal SV could evolve into a blocking-like structure. For this purpose, we needed time-evolving basic states which, although starting from the correct initial state and representing a realistic atmospheric evolution, did not lead to a block (hopefully allowing the perturbation to do the job!). The integrations of the primitive-equation T63 model described in MMP satisfied all these requirements, and therefore were chosen as basic-state trajectories in both case studies.

In order to concentrate our attention on the role of the basic state and to investigate the possible importance of non-linear self-interactions of the perturbation eddies, we show here results of different integrations using one single perturbation for each case, namely the fastest growing 12-hour SVs computed with the QG model

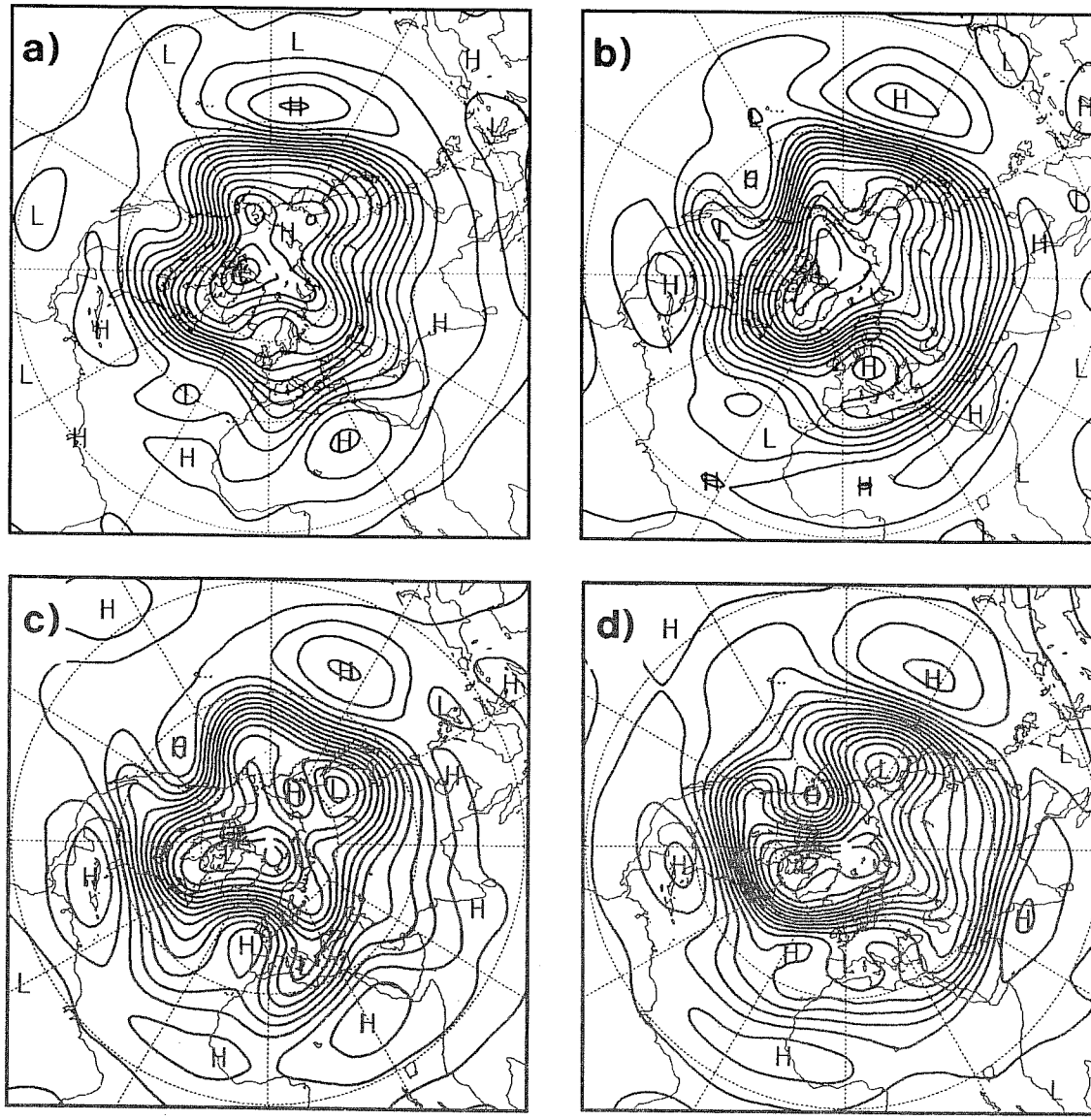

Fig. 14 5-day means of 500 hPa streamfunction centred on 2 December 1988 (a) and 27 January 1989 (b); c-d): as in a) and b) respectively, but centred eight days later. Contour interval $6.\cdot 10^6$ m^2/s.

using the initial 5-day means shown in Fig. 13 a-b as time-independent basic states. Four separate integrations have been carried out for each case. The first one is a linear integration using the initial 5-day mean as fixed basic states. The second integration is again linear, but uses the time-evolving basic state derived from the primitive-equation T63 forecasts; here, no time filtering is applied to the basic state, although the streamfunction fields are truncated at the spatial resolution (T21) of the QG model. The third and fourth runs are nonlinear integrations of the full QG model, in which the initial state is perturbed by the 12-hour SV with positive and negative sign, and a global rms wind amplitude of 1 m/s.

As discussed in section 3, in order to run the QG model in non-linear mode is necessary to provide some appropriate forcing through the PV source terms S_i in Eq. 12. Since we wanted the unperturbed QG trajectory to remain very close to the primitive-equation T63 trajectory used for the linear calculations, we first run the unperturbed QG model adding to the rhs of Eq. 12 a-b-c a 'relaxation' term of the type:

$$S_i(t) = \alpha \, (q_i - q_i^*)$$

where q_i is the QG PV at level $i = 1, 2, 3$, q_i^* is the corresponding PV computed from T63 fields, and α a relaxation coefficient equal to (6 hours)$^{-1}$. The time evolving source terms $S_i(t)$ computed from the unperturbed relaxation run were stored and then applied to the perturbed integrations (without modification, so that no relaxation acted on the perturbations).

The evolution of perturbation amplitude with time for the different integrations using the optimal 12-hour SV is given in Table 6. It is interesting to note that at day 8, in all cases considered, the amplitude of the perturbation on the 27 January basic state is larger than the amplitude of the equivalent perturbation for the 2 December basic state. This would appear to be consistent with the differences in the ECMWF forecast error, and also with calculations performed with the cluster centroid basic states.

On the other hand, there are substantial differences in the amplification rates between the fixed and evolving basic states, and between the linear and nonlinear integrations. For example, at day 8 the linear amplification of the perturbations on the time evolving basic state is about twice that on the fixed basic state. This highlights the importance of the interaction between the perturbation and the basic-state synoptic eddies, largely filtered out by time-averaging or compositing. The effect of nonlinearity on the time-evolving basic state is to reduce perturbation growth, particularly after day 4; this appears to be the consequence of saturation arising from the dynamical conservation properties of the equations of motion.

Fig. 15 shows the SV perturbation at day 8 for the 27 January basic states, firstly for the linear evolution with fixed basic state (first column), secondly for the linear evolution with time-evolving basic state (second

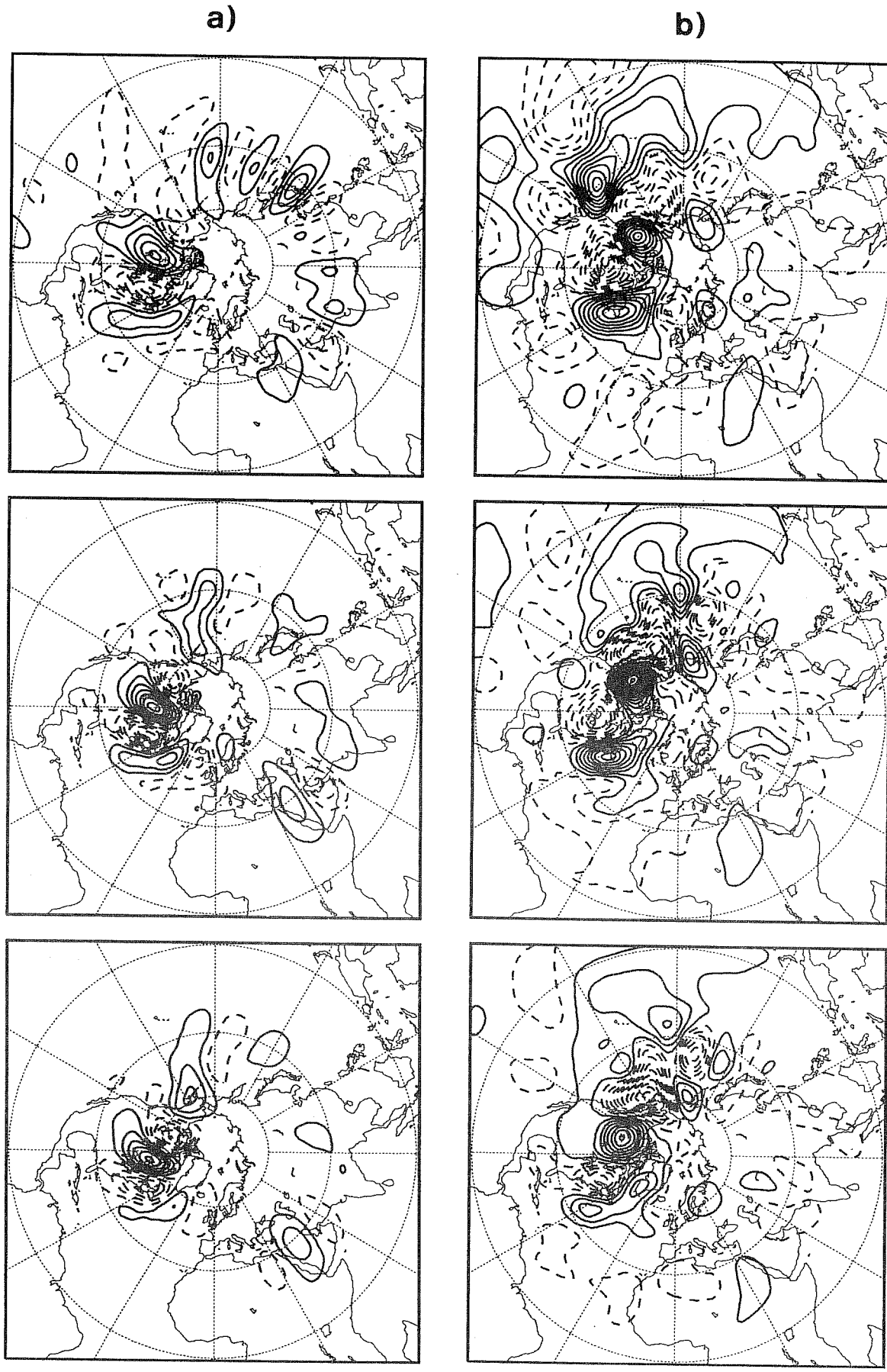

Fig. 15 Perturbation at day 8 at 200 hPa (top), 500 hPa (centre), and 800 hPa (bottom) obtained from different integrations of the optimal 12-hr SV for the 27/1/1989 case. Column a): from linear integration on a fixed 5-day mean basic state; column b) from linear integration on a time evolving basic state; column c): from a non-linear integration on a time evolving basic state, starting with positive sign; column d): as in c) but starting with opposite sign. Contour interval $15.\cdot 10^6$ m^2/s.

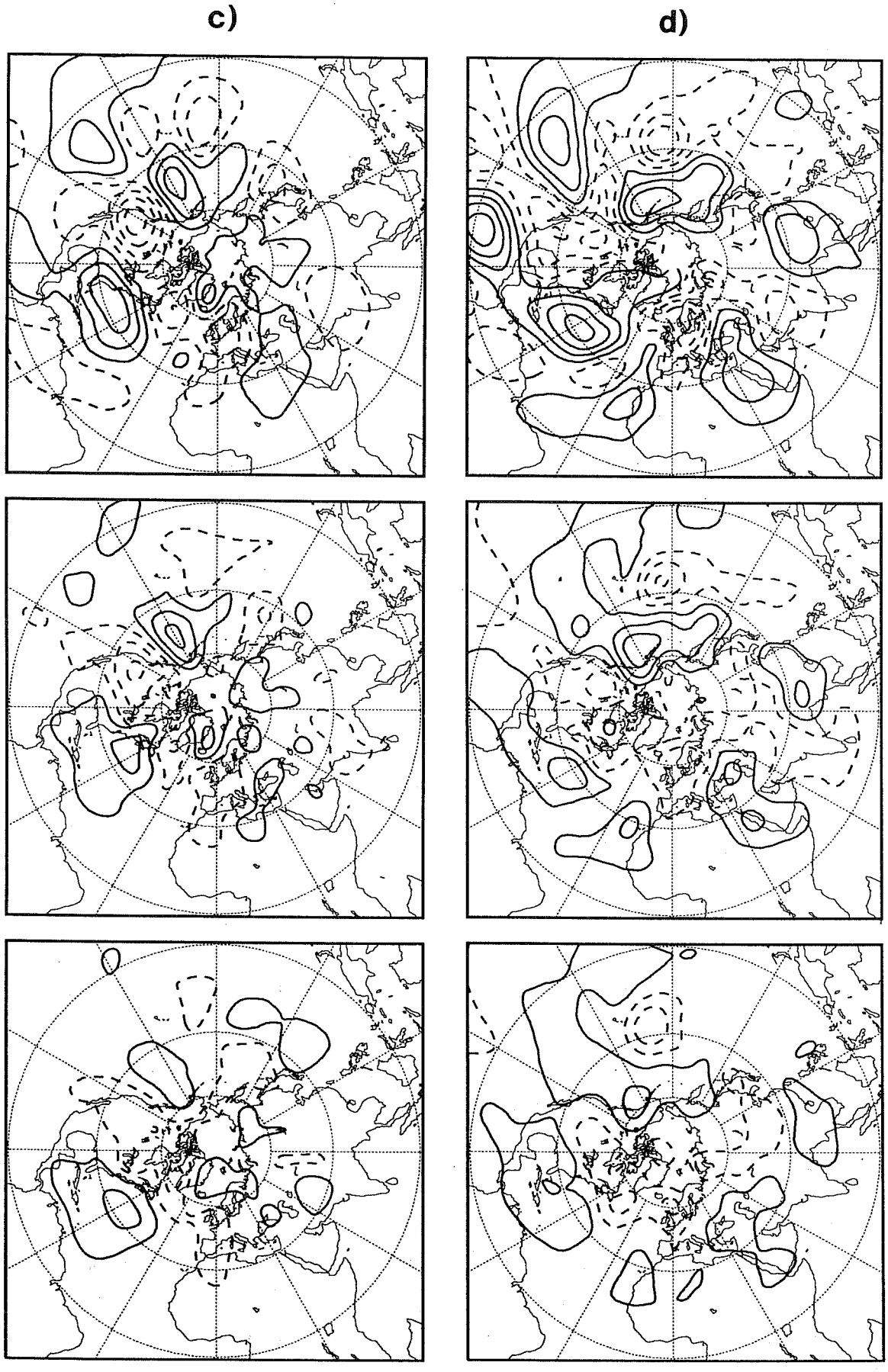

Fig. 15 continued.

column), and finally for the nonlinear evolution with time-evolving basic state (third and fourth column for positive and negative sign). All three levels of the QG model are shown.

There is a fundamental difference in the vertical structure of the perturbations between the two linear calculations. In particular, with the fixed basic state, at day 8 the perturbation retains a westward tilt with height consistent with its asymptotic normal-mode tendency. On the time-evolving basic state, the structure of the perturbation is essentially equivalent barotropic. Indeed between days 4 and 8, the phase of the perturbation has become much more stationary than with the fixed basic state.

This difference can be related to the fact that the time-evolving basic state has no normal mode structure. It would appear that the interaction of the perturbation with the (time-evolving) synoptic eddies in the basic state is responsible for generating an equivalent barotropic structure in the linear perturbation. These calculations highlight the fundamental difference between the nature of the error growth in a time-evolving basic state and in an average, smoothed field (either a time mean or a cluster centroid) which retains only the large-scale features of this basic state.

The nonlinear calculation also generates an equivalent barotropic structure at day 8. It is interesting to note the overall increase in the dominant horizontal scale of the perturbation, indicative of a nonlinear upscale energy cascade. A further indication of non-linearity is that initial perturbations with opposite sign have produced positively correlated patterns over the Pacific-North American region. In particular, the perturbation with negative sign (which has a larger amplitude at day 8) has produced a clear blocking-type dipole just east of the dateline between 60°N and 30°N, in agreement with the observed development.

7. CONCLUSIONS

In this study, we have analysed measures of barotropic and baroclinic instability computed from the growth rates of normal modes and SVs of time-independent basic states (climatological flow and two regime centroids), and we have compared the growth of baroclinic perturbations in fixed and time-evolving basic states. Our main conclusions can be summarised as follows.

1) For integration times shorter or comparable with the theoretical limit of atmospheric predictability (about 15 days), in both a barotropic and a 3-level QG model the growth rates of the optimal SVs are significantly larger (up to one order of magnitude) than the growth rates of the most unstable normal mode for any given basic state. Indeed, the normal mode growth rate in the baroclinic model could not justify the observed value of about 2 days for the doubling-time of small errors in numerical weather predictions; for the optimal SVs, amplitude can double in less than 12 hours.

2) Indices of barotropic instability deduced from the linear growth of optimal SVs superimposed on fixed basic states corresponding to cluster centroids show more difference between positive and negative PNA regimes (the latter states being more unstable) than corresponding indices of baroclinic instability. However, we have shown that the linear evolution of baroclinic perturbations on a smooth basic state retaining only planetary-scale features cannot properly reproduce the fundamental process through which such perturbations generate regime transitions: namely, the upscale energy cascade which transfers energy from the synoptic-scale to the planetary-scale waves. If one assumes that these baroclinic calculations are only relevant to cases of regime persistence, then the agreement with observed errors is good. On the other hand, barotropic SVs are optimised to extract kinetic energy from the subtropical flow and transfer it to midlatitude planetary-scale eddies; they seem able to generate regime transitions.

3) The agreement between linear baroclinic instability indices and error growth in cases of regime transitions is much improved when synoptic-scale eddies are included in the basic state, using time-averages over short periods of time or, more appropriately, an unsmoothed time-evolving basic state. In these cases, interactions between basic state and perturbation synoptic-scale eddies can occur. With time-evolving basic states, after a few days the perturbations develop an equivalent barotropic structure, which is characteristic of large-scale anomalies.

4) If baroclinic SVs with initial amplitude comparable to analysis errors are allowed to evolve non-linearly over a time-dependent basic state, then the non-linear self interaction of the perturbation can reinforce the barotropic energy transfer to large-scale, equivalent barotropic structures. We have shown that onset of a Pacific block in one of our case studies can be well simulated by the non-linear development of a SV optimised to have the fastest growth in the initial 12-hour time interval.

These results allow us to devise a strategy to use SVs in non-linear ensemble predictions. Baroclinic SVs, even if optimised for short time intervals (when the growth of initial errors can be assumed to be linear), develop in an efficient and realistic way when superimposed on time-evolving basic states. The results of ensemble-forecast experiments with a T63 primitive equation model, using QG SVs as initial perturbations, are reported in a companion paper (MMP), and provide encouraging support for this dynamically-based approach to ensemble predictions.

APPENDIX A. Dissipative terms in the QG model.

In Eq. 12, the linear terms representing the PV tendencies due to dissipative processes have been synthetically indicated as D_1, D_2, D_3, where the subscript i = 1, 2, 3 refers to the pressure levels (200, 500 and 800 hPa respectively). These terms include contributions from temperature relaxation, Ekman dissipation and horizontal diffusion:

A.1) $$-D_1 = +TR_{12} - H_1$$

A.2) $$-D_2 = -TR_{12} + TR_{23} - H_2$$

A.3) $$-D_3 = -TR_{23} - EK_3 - H_3$$

The term:

A.4) $$TR_{12} = \tau_R^{-1} R_1^{-2} (\psi_1 - \psi_2)$$

represents the effect of temperature relaxation between levels 1 and 2, with a radiative time scale τ_R = 25 days;

A.5) $$TR_{23} = \tau_R^{-1} R_2^{-2} (\psi_2 - \psi_3)$$

is the corresponding term for temperature relaxation between levels 2 and 3.

Ekman dissipation is expressed as the vorticity tendency due to a linear drag on the 800 hPa wind:

A.6) $$EK_3 = (a \cos\phi)^{-1} \left[\frac{\partial}{\partial\lambda} (k(\lambda, \phi, h)\, v_3) - \frac{\partial}{\partial\phi} (k(\lambda, \phi, h)\, u_3 \cos\phi) \right]$$

where λ is longitude, ϕ latitude, h the orographic height, a the average Earth radius, and

$$u_3 = -a^{-1} \frac{\partial\psi_3}{\partial\phi}, \qquad v_3 = (a \cos\phi)^{-1} \frac{\partial\psi_3}{\partial\lambda}$$

The drag coefficient k is dependent on the land-sea mask and on the orographic height:

A.7) $$k(\lambda, \phi, h) = \tau_E^{-1} [1 + \alpha_1 LS(\lambda, \phi) + \alpha_2 FH(h)]$$

where:

τ_E = 3 days;

$\alpha_1 = \alpha_2 = 0.5$;

$LS(\lambda, \phi)$ = fraction of land within a grid-box;

$FH(h) = 1 - \exp[-h/(1000\ m)]$.

Since LS and FH vary between 0 and 1, k varies between (3 days)$^{-1}$ over the oceans, (2 days)$^{-1}$ over zero-altitude land, and about (1.5 day)$^{-1}$ over mountain areas higher than 2000 m. (The grid-point values of

orography and land-sea mask are derived from the spectral T21 representation of the actual high-resolution fields, and therefore represent averages over an area of the order of $(1000\ \text{km})^2$.) If one neglects the spatial variations in the drag coefficient by setting $\alpha_1 = \alpha_2 = 0$, Eq. A.7 reduces to the simple form:

A.8) $$EK_3 = \tau_E^{-1} \nabla^2 \psi_3$$

Finally, at each pressure level, the time-dependent component q'_i of PV (i.e., PV minus planetary vorticity and orographic component) is subject to a scale-selective horizontal diffusion:

A.9) $$H_i = c_H \nabla^8 q'_i$$

where the coefficient

A.10) $$c_H = \tau_H^{-1} a^8 (21 \cdot 22)^{-4}$$

is such that spherical harmonics of total wavenumber 21 are damped with time scale $\tau_H = 2$ days.

APPENDIX B. Computation of streamfunction cluster centroids.

The atmospheric clusters defined by *Molteni et al.* (1990) were computed from a 32-winter sample of 5-day mean eddy anomalies of 500 hPa height covering the area 20°N to 90°N. For this study, we needed global, 3-dimensional streamfunction fields such that their eddy anomalies at 500 hPa, when converted into geopotential height eddies, were as close as possible to the original cluster centroids; however, we also wanted the zonal mean and tropical flow, and the flow at other pressure levels, to be dynamically (and statistically) consistent with the pattern of the 500 hPa northern extratropical eddies.

We therefore decided to construct our streamfunction centroids as the sum of a climatological field (the average of ECMWF analyses in January and February 1984 to 1989) and an anomaly defined as a weighted average of the departures of 5-day mean streamfunction fields (selected in the same period) from the climatology. Each 3-dimensional field was defined at the levels of 200, 300, 500 and 800 hPa (the three levels of the QG model plus the equivalent barotropic level).

The selection of fields and the definition of weights were performed as follows:

1) for each 5-day mean streamfunction fields in our 12-month sample, the streamfunction anomaly at 500 hPa was converted into a geopotential height anomaly by solving a linear balance equation;

2) the zonal mean was removed from the 500 hPa height anomalies, which were then projected onto the same empirical orthogonal functions (EOF's) used by *Molteni et al.* (1990) for their cluster analysis;

3) for any given cluster centroid, the distance from each eddy anomaly was computed in the EOF space, and the 30 closest fields (out of 72) were selected;

4) a non-linear least-square-fit routine was used to find 30 (positive) weight so that the weighted average of the 30 selected eddy anomalies of 500 hPa height was as close as possible to the cluster centroid.

Once the weights were found for each cluster, they were applied to the 3-dimensional streamfunction anomalies of the 30 selected 5-day means; the composite anomaly was then superimposed to the climatology to get the full-field streamfunction centroid.

TABLE 1: Amplification factor (relative to the initial amplitude) of the most unstable normal mode (NM) and optimal singular vector (SV) calculated with the barotropic model and the climatological winter basic state in Fig. 1 (first two columns), and with the QG model and the climatological winter basic state in Fig. 4 (last two columns).

	Barotropic NM	Barotropic SV	Baroclinic NM	Baroclinic SV
Integr. time:				
12 hours	1.00	1.6	1.1	2.2
1 day	.99	2.3	1.2	3.8
2 days	.99	3.4	1.4	7.4
4 days	.98	4.7	1.8	15.0
8 days	.96	5.1	3.3	25.8
16 days	.92	4.7	11.0	58.2

TABLE 2: Amplification factor (relative to the initial amplitude) of n-day optimal mode (where n=1/2, 1, 2, 4, 8) evaluated at days 1/2, 1, 2, 4, 8, calculated with the barotropic model with climatological basic state.

Optim. time:	12 hours	1 day	2 days	4 days	8 days
Integr. time:					
12 hours	1.6	1.5	1.3	1.2	1.1
1 day	2.1	2.3	2.0	1.6	1.4
2 days	2.0	2.8	3.4	2.9	2.2
4 days	1.4	2.1	3.5	4.7	3.7
8 days	0.8	1.2	2.3	3.4	5.1

TABLE 3: As Table 2 but for the QG model.

Optim. time:	12 hours	1 day	2 days	4 days	8 days
Integr. time:					
12 hours	2.2	2.1	1.8	1.7	1.3
1 day	3.5	3.9	3.5	3.0	2.1
2 days	5.4	6.6	7.4	6.2	3.8
4 days	8.3	10.0	12.0	15.0	9.0
8 days	7.1	9.7	12.1	17.0	25.8

TABLE 4: Amplification factor (relative to the initial amplitude) of the most unstable normal mode (NM) and optimal singular vector (SV) calculated with the barotropic model for cluster 2 flow (first two columns), and for cluster 5 flow (last two columns).

	Cluster 2		Cluster 5	
	NM	SV	NM	SV
Integr. time:				
12 hours	1.0	1.7	1.0	1.6
1 day	1.0	2.5	1.1	2.3
2 days	1.1	3.8	1.2	3.7
4 days	1.2	5.3	1.3	6.3
8 days	1.5	5.9	1.7	11.2

TABLE 5: As Table 4 but for the QG model.

	Cluster 2		Cluster 5	
	NM	SV	NM	SV
Integr. time:				
12 hours	1.1	2.3	1.1	2.2
1 day	1.1	4.1	1.2	3.8
2 days	1.2	8.2	1.3	7.2
4 days	1.6	17.7	1.8	14.0
8 days	2.5	25.7	3.2	28.8

TABLE 6: Amplification factors (relative to the initial amplitude) of the optimal 12-hour SV for the 2/12/1988 and 27/1/1989 case studies, computed from a linear integration on a fixed 5-day-mean basic state (FL), linear integration on a time-evolving basic state (TL), and non-linear integrations on a time-evolving basic state with positive (TN+) and negative (TN-) sign of the initial SV perturbation (initial amplitude = 1 m/s).

Integr. time	12 hours	1 day	2 days	4 days	8 days
2 Dec. 1988:					
FL	2.2	3.5	5.3	6.8	11.9
TL	2.3	3.8	5.6	8.1	25.3
TN+	2.3	3.6	4.2	5.7	8.2
TN-	2.3	3.7	4.6	6.2	9.7
27 Jan. 1989:					
FL	2.4	3.8	5.6	8.2	19.0
TL	2.5	3.8	5.2	9.8	30.7
TN+	2.4	3.5	3.9	6.7	11.2
TN-	2.4	3.9	6.4	10.6	14.2

REFERENCES

Borges, M.D and D.L. Hartmann, 1991: Barotropic instability and optimal perturbations of observed non-zonal flows. Submitted to J.Atmos.Sci.

Chen, W.Y., 1989: Another approach to forecasting forecast skill. Mon.Wea.Rev., 117, 427-435.

Cheng, X. and J.M. Wallace, 1991: Cluster analysis of the northern hemisphere wintertime 500mb height field. Submitted to J.Atmos.Sci.

Farrell, B.F., 1988: Optimal excitation of neutral Rossby modes. J.Atmos.Sci., 45, 163-172.

Farrell, B.F., 1989: Optimal excitation of baroclinic waves. J.Atmos.Sci., 46, 1193-1206.

Ferranti, L., T.N. Palmer, F. Molteni and E. Klinker, 1990: Tropical-extratropical interaction associated with the 30-60 day oscillation and its impact on medium range and extended-range prediction. J.Atmos.Sci., 47, 2177-2199.

Lacarra, J.-F. and O. Talagrand, 1988: Short-range evolution of small perturbations in a barotropic model. Tellus, 40A, 81-95.

Legras, B. and M. Ghil, 1985: Persistent anomalies, blocking and variations in atmospheric predictability. J.Atmos.Sci, 42, 433-471.

Lorenz, E.N., 1965: A study of the predictability of a 28-variable atmospheric model. Tellus, 17, 321-333.

Lorenz, E.N., 1985: The growth of errors in prediction. Turbulence and Predictability in Geophysical Fluid Dynamics and Climate Dynamics, North Holland, Amsterdam, 243-265.

Malguzzi, P., A. Trevisan and A. Speranza, 1990: Statistics and predictability for an intermediate dimensionality model of the baroclinic jet. Ann.Geophys., 8, 29-36.

Marshall, J. and F. Molteni, 1992: Towards a dynamical understanding of planetary-scale flow regimes. Submitted to J.Atmos.Sci.

Molteni, F., S. Tibaldi and T.N. Palmer, 1990: Regimes in the wintertime circulation over nothern extratropics. I Observation evidence. Q.J.R.Meteor.Soc., 116, 31-67.

Molteni, F. and S. Tibaldi, 1990. Regimes in the wintertime circulation over northern extratropics. II Consequences for dynamical predictability. Q.J.R.Meteor.Soc., 116, 1263-1288.

Mukougawa, H., M. Kimoto and S. Yoden, 1991: A relationship between local error growth and quasi-stationary states: case study in the Lorenz system. J.Atmos.Sci., 48, 1231-1237.

Mureau, R., F. Molteni, T.N. Palmer, 1992: Ensemble prediction using dynamically-conditioned perturbations. To be submitted to Q.J.R.Meteor.Soc.

Noble, B. and J.W. Daniel, 1977: Applied Linear Algebra. Prentice-Hall, Inc., USA, 477pp.

Palmer, T.N., 1988: Medium and extended-range predictability and stability of the Pacific/North American mode. Q.J.R.Meteor.Soc., 114, 691-713.

Palmer, T.N. and S. Tibaldi, 1988: On the prediction of forecast skill. Mon.Wea.Rev., 116, 2453-2480.

Parker, T.S. and L.O. Chua, 1989: Practical numerical algorithms for chaotic systems. Springer-Verlag. New York. 348pp.

Simmons, A.J., J.M. Wallace and G.W. Branstator, 1983: Barotropic wave propagation and instability, and atmospheric teleconnection patterns. J.Atmos.Sci., 40, 1363-1392.

Wallace, J.M. and D.S. Gutzler, 1981: Teleconnections in the geopotential height field during the northern hemisphere winter. Mon.Wea.Rev., 109, 784-812.

Yoden, S. and M. Nomura, 1991: Local Lyapunov stability analysis and its application to atmospheric predictability. Submitted to J.Atmos.Sci.

Zhang, Z., 1988: The linear study of zonally asymmetric barotropic flows. PhD Thesis. Reading University. UK.